Optimal Placement of Binary Actuators in Deformable Optical Systems

by

Roman Geykhman

B.S.E. in Electrical Engineering, University of Pennsylvania (2007)
B.A. in Mathematics, University of Pennsylvania (2007)

Submitted to the Department of Mechanical Engineering
in partial fulfillment of the requirements for the degree of

Master of Science in Mechanical Engineering

at the

MASSACHUSETTS INSTITUTE OF TECHNOLOGY

June 2011

Author .....
Department of Mechanical Engineering
May 6, 2011

Certified by .....
Steven Dubowsky
Professor
Thesis Supervisor

Accepted by .....
David E. Hardt
Graduate Officer

Optimal Placement of Binary Actuators in Deformable Optical Systems

by

Roman Geykhman

Submitted to the Department of Mechanical Engineering
on May 6, 2011, in partial fulfillment of the
requirements for the degree of
Master of Science in Mechanical Engineering

Abstract

Recently, exploration has been conducted into the applicability of binary mechatronics to active figure correction in large optical systems such as space telescopes and ground-based solar-thermal concentrators. This Thesis will continue this exploration. The information-theoretic requirements of the corrective commands required in active optics will be explored to understand the dimensionality of the continuous workspace sampled by binary actuation. In both the minimal expected error and the minimal computation time sense, the optimal discrete workspace is the uniform discrete distribution. A rigorous analogy between binary mechatronics and discrete random variables will be used to show that this optimal workspace is achievable by a linear superposition of actuators with exponentially decreasing influences on the optical surface. It will be proven that elasticity can be exploited to construct mechanisms where constant magnitude actuators exhibit exponentially decaying influences on certain parts of the mechanism, allowing for designs where individual binary actuators correspond to binary bits of the required deformation. A planar truss mechanism designed with this philosophy will be presented and shown to have independent kinematic control of multiple adjacent displacements on its top side. Finally, this design will be shown extend to three dimensions in a manner applicable to optical figure correction. Due to the complexity of mechanisms that meet the optimality criteria, only theoretical analysis will be presented.

Thesis Supervisor: Steven Dubowsky
Title: Professor

Disclaimer: This work is sponsored by the Department of the Air Force under Air Force Contract #FA8721-05-C-0002. Opinions, interpretations, conclusions and recommendations are those of the author and are not necessarily endorsed by the United States Government.

Acknowledgments

I have many people to thank for helping me get this far.

First, my parents Oskar and Eugenia Geykhman and my grandparents Viktor Serman and Liliya Kamchatova, who raised me to become an engineer. It is through their kind but firm hand, their scrupulous attention to my upbringing, and their tireless efforts at so many tasks, both grand and petty, that I am where I am today.

Rena Zheng, whose voice never failed to lift my soul.

My friends and colleagues, who helped to keep me grounded in my purpose.

My fellow students at the MIT Field and Space Robotics Laboratory for the opportunity I have had to work in their company. I owe specific, but not exclusive, gratitude to Amy Bilton, Paul Lee, and Lily Li for their invaluable assistance in my research, and to Leah Kelley for being a good classmate and a friendly ear. Of course I must acknowledge Prof. Steven Dubowsky for presenting me with an interesting open problem, and for giving me the latitude to explore it.

I must express gratitude to my supervisors at Lincoln Laboratory, especially Dr. Susan Andrews, Dr. Jack Fleischman, and Dr. Stephen Hunt who encouraged and supported my aspirations from the beginning, and tolerated my absence during my studies.

Finally, I would like to acknowledge the financial support of the Lincoln Laboratory Graduate Education Committee through the Lincoln Scholars Program and of the David Karp Memorial Foundation for making my studies possible.

To everyone: Thank You.

Contents

List of Figures

Chapter 1

Introduction

The Digital Revolution in electronics stemmed from a single core idea: that the random errors and noise in linear analog electronics could be traded for discretization error and higher component count in more accurate and precise digital circuits. A similar idea, termed Digital or Binary Mechatronics, is applicable to some mechanical systems, where the expense and manufacturing precision required to construct a single continuous actuator can be traded for a larger number of inexpensive discrete actuators [3].

Over the last two decades, this idea has been explored by Chirikjian [3], Ebert-Uphoff [10] [11], Lees [16] [17], and Sujan [27] primarily in the context of constructing robot manipulators actuated by many binary piston-like actuators rather than a few continuous rotation or piston joints. Two such mechanisms are shown in Figure 1-1. Additionally, DeVita and Plante investigated parallelized arrangements of binary actuators in a compliant mechanism for precise positioning in medical imaging [7], [8].

Recently, Lee, Bilton, and Dubowsky introduced the idea of employing binary mechatronics in active figure correction for optical systems such as solar-thermal

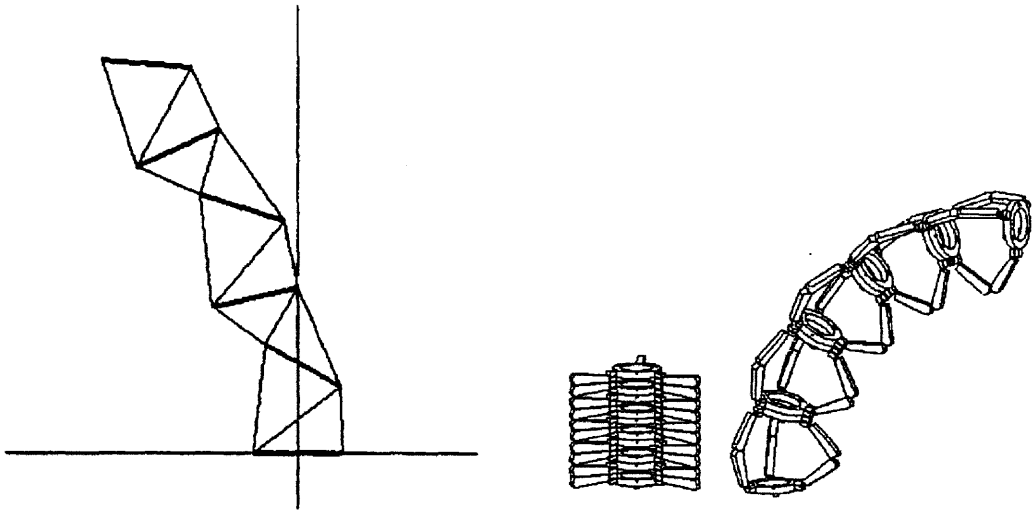

Figure 1-1: Serial Chain Binary Actuated Mechanisms. Left: Chirikjian's VGT Manipulator [3]. All truss members are binary pistons. Right: Sujan, Lichter, and Dubowsky's BRAID Manipulator [27]. All joints are binary rotation actuators.

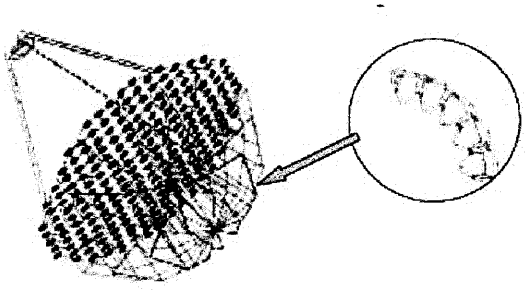

Figure 1-2: Dubowsky's Binary Large Imaging Space Structure Concept [14]. Segmented mirror supported by binary mechatronic truss.

concentrators [15] and extremely large orbiting telescopes [14] by embedding large numbers of binary actuators inside the support structure of the primary reflecting surface, as shown in Figure 1-2. Unlike Chirikjian's serial manipulators, the actuator arrangements in these structures are naturally more parallel, and require a different mathematical framework to design, analyze, and control them.

The purpose of this Thesis is to continue the theoretical exploration of the applicability of binary mechatronics for use in large optical systems. Specifically, this Thesis will mathematically prove a tight lower bound on the number of binary actuators required to achieve a specified accuracy in a general binary-actuated system, develop a design paradigm that exploits mechanism elasticity to both achieve that lower bound and allow for constant-time inverse kinematics, and will present an example design that uses this framework in a way that that is directly applicable, with a some caveats, to the control of a multi-d.o.f. deformable optical surface for use in active optics, large microwave antennas, and potentially large orbiting collectors.

The remainder of this chapter will build the context from the two fields intersecting in this line of research. First, a review of figure correction requirements in state-of-the-art parabolic concentrator systems, that operate in both the coherent and incoherent regime, will build the case that in almost all applications, the shape error in a parabolic reflecting surface requires a correction by an actuator arrangement capable of controlling a relatively large number of independent degrees of freedom distributed over the extent of the reflecting surface. Second, a detailed review of the state of the art in binary mechatronics will lay out the particular subtleties involved in designing and controlling binary actuated mechanisms. Specific attention will be paid to methods of inverse kinematics and system accuracy. The purpose of the guided exposition will be to build up the necessary context for optimality considerations in the use of binary mechatronics for control of deformable

optical surfaces, the theoretical exploration of which is the original contribution of this Thesis.

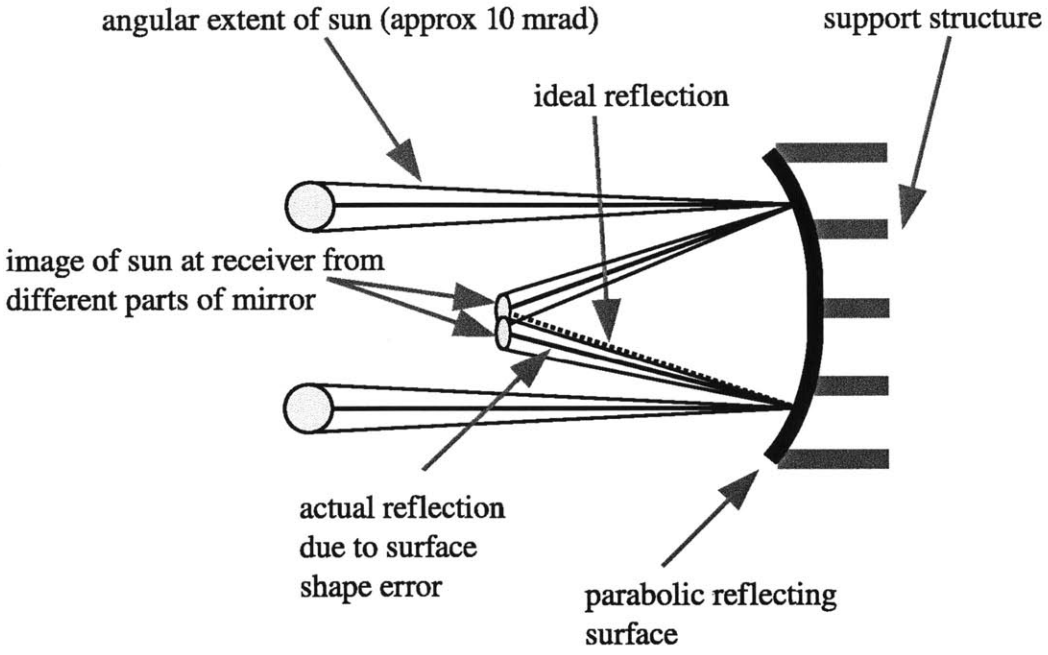

Figure 1-3: Geometry of Incoherent Concentrating Optics. Because the nonzero angular diameter of the sun will focus to some finite extent on the receiver, the geometric tolerances on the surface are dominated by the desired overlap between images from different parts of the mirror. If, for example, 99% overlap ($< 1\%$ loss) is specified, then the angle of the mirror must be accurate to 0.1 mrad (0.01×10 mrad) over the whole mirror, necessitating support structure accuracy equivalent to 100 μm per meter.

1.1 The Need for Control of Deformable Optical Surfaces

The surface shape tolerances for parabolic concentrating collectors depend on the application and operating wavelength of the incident radiation. Incoherent regime solar-thermal concentrators tend to have the loosest requirements. The surface quality is determined purely by gross geometric co-alignment of distinct regions of the surface. As shown schematically in Figure 1-3, the tolerance on the mirror support geometry generally requires support structure accuracy on the order of tenths of millimeters. In coherent systems such as astronomical telescopes and microwave radar antennas, on the other hand, the surface tolerances required are on the order of a small fraction of the operating wavelength (tens of *nano*meters for micron-wavelength visible band systems) over the entire aperture in order for the incoming signal wavefront to combine from reflections over the entire aperture at the instrument focus with minimal destructive interference.

Wavefront disturbances in coherent systems can be broadly divided into mechanical imperfections in the instrument itself and (in optical telescopes) external disturbances from the atmosphere. Atmospheric disturbances are generally high in their temporal frequency (upwards of 30 Hz [28]) and in their spatial frequency when compared with the length scale of a large primary mirror. As indicated in Figure 1-4, they are usually measured and canceled out with a dedicated deformable mirror several elements down the optical path from the primary in an arrangement termed *adaptive optics.*

The mechanical disturbances, common to coherent and incoherent systems, result from gravitational and thermal loading of the primary mirror and its support

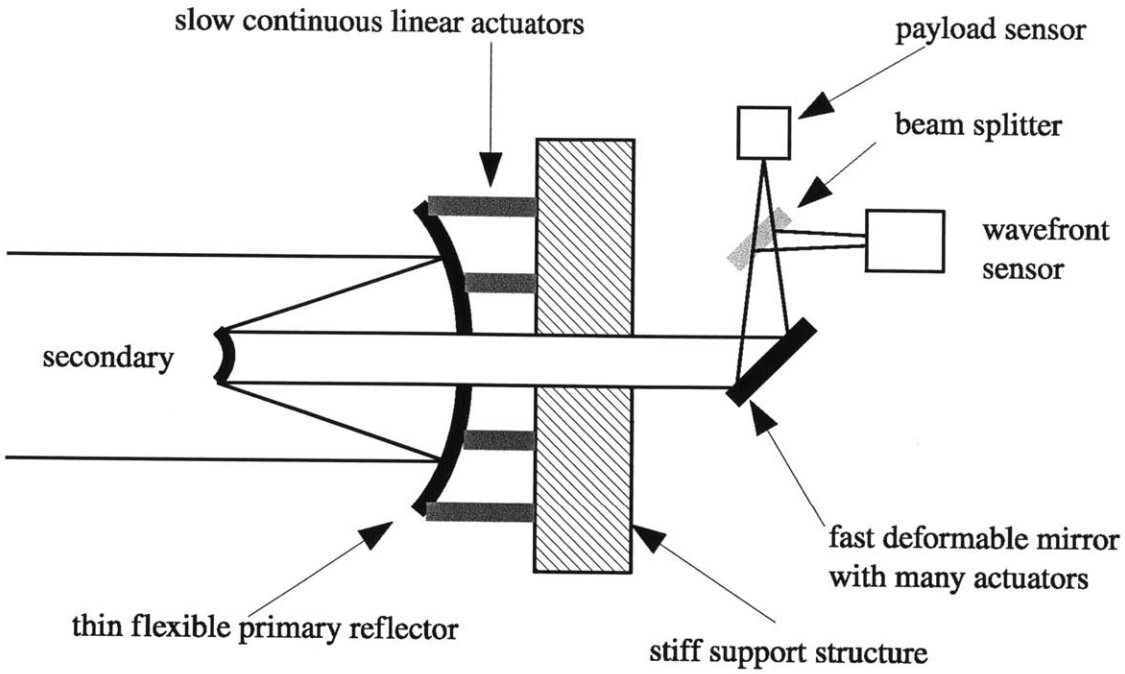

Figure 1-4: Actuator Functions and Locations in Ground-Based Astronomical Telescopes

structure. While a great deal of mechanical design effort and precision fabrication goes into minimizing these disturbances, at large mirror sizes and small wavelengths, it becomes necessary to remove them with closed-loop control of the optical surface rather than careful passive engineering [1], in a method termed *active optics.* Given the slow rate of motion and temperature changes typically encountered during operations of large astronomical observatories and sun-tracking solar concentrators, these disturbances are slow in temporal frequency, and in instances where they are actively controlled against, require closed loop cycles times between 500 msec [31] and 60 seconds [12].

The research for this Thesis was originally motivated by the need to correct mechanical disturbances in the primary reflectors of large orbiting telescopes, and the bulk of this document will focus on correcting slow timescale, large scale, mechanical disturbances in the primary reflector support structure. To that end, this section will provide some historical background and mechanical intuition for the challenges in constructing large, precise paraboloids, the characteristics of the errors active optics is meant to correct, and some general properties of continuously-actuated active optics systems currently deployed in large telescopes. The purpose of the exposition will be both to characterize the design requirements for binary mechatronic active optics system, and to make the case that the current state-of-the art, multi-d.o.f. actuator layout presents the most natural jumping-off point to move from a continuous actuator to a binary actuator design.

1.1.1 The Problem of Primary Mirror Rigidity

As ground-based and space-based telescopes have increased in diameter, the geometric tolerance requirements on the primary reflecting surface have become harder to meet with purely passive design methods of material selection and support structure geometry. The challenge comes from the requirement that the primary reflecting surface be both locally smooth *and* globally accurate to sub-wavelength tolerances.

While the millimeter-wave radar regime, and associated tolerances of 100-μm surface accuracy is sufficiently loose to allow 40-meter class antennas to be constructed as purely passive rigid structures [19], the sub-micron optical regime presents significant challenges for even much smaller aperture diameters. To cite a prominent example from astronomy, in the final integration of the 200-inch (5m) monolithic primary mirror of the Hale Telescope, considerable effort had to be expended to

eliminate mirror surface deflections of several tens of μinches ($\approx 0.5\mu$m, approximately the optical wavelength) that resulted from gravity-induced deformation of the 20-inch outer band of the mirror over the range of motion of the mirror cell [2].

While small amateur-scale optical telescopes with mirror diameters on the order of approximately 1/10 of a meter almost exclusively employ monolithic glass mirrors that are aligned to the secondary optics with three-point kinematic mounts, larger reflectors require distributed support structures under the surface of the mirror to maintain their figure. The Hale Telescope, for instance, employs a 36-point mirror support that "floats" the mirror [1]. Each support point is a passive mechanical balance that is carefully tuned to exactly counter in magnitude and direction the pull of gravity on the mirror in its vicinity.

In the newer over 5-meter telescopes constructed from the 1980's onward, however, the size of the primary reflectors exceeded the point where careful engineering and calibration could ensure that the surface tolerances could be achieved with purely passive mechanisms [1].

The construction of the Keck Telescopes in Hawaii and the Very Large Telescopes in Chile demonstrate two flavors of the solution to the surface figure problem past the 5 meter aperture size. The Keck primary mirror, shown in Figure 1-5, is composed of 36 1.8-meter hexagonal segments, each figured as an off-axis paraboloid. While the individual segments are designed to be rigid enough to hold their shape over the range of motion and temperature experienced during science operations [1], the supporting truss deforms over the range of motion of the elevation axis of the telescope, necessitating active closed loop position control of the segments themselves relative to each other and relative to the absolute desired figure of the reflector.

The alternate philosophy, employed in the 8.2 meter Very Large Telescopes in Chile has been to construct thin monolithic *flexible* primary mirrors, and to distribute

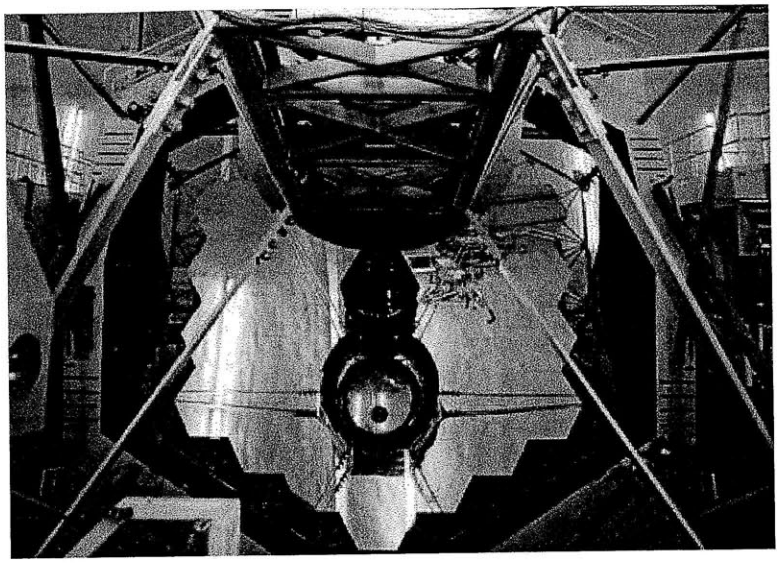

Figure 1-5: Segmented Primary Mirror on the Keck Telescope. The interface between each segment edge requires sub-wavelength position alignment over the entire range of motion of the mirror. Courtesy W. M. Keck Observatory [31].

many actuators under their surface. The VLT mirrors each use 150 active supports (about three per square meter) [12]. The supports are shown in Figure 1-6.

In both of these designs, a closed loop controller, measuring the absolute alignment and figure of the entire mirror surface, independently controls the force applied to many support points distributed over the extent of the primary.

1.1.2 Spatial Frequencies of the Disturbance and Locality of Actuator Influences on the Surface Figure

At this point, an important and subtle question must be addressed. Given the smoothly varying deformations associated with gravitational and thermal loading of the primary mirror, what sort of actuation is required to correct it to the required tolerance of several tens of nanometers in the optical case and several hundred microns

Figure 1-6: Mirror Support Structure for ESO 8.2-meter Telescope. Active supports are visible sticking up from the backplane. Observe the large number of degrees of freedom in the active support structure. Image Credit: ESO [12]

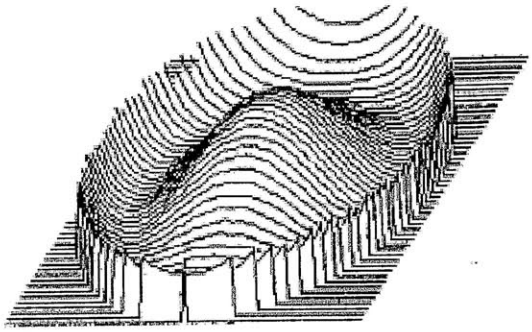

Figure 1-7: Normalized Deformation Shape of a Circular Mirror In Response to Uniform Thermal Loading on One Surface [20].

in the solar-thermal case? This section will show that even though the disturbances are smoothly varying and have low "information content," any practical active correction system will require *many independent degrees of freedom* to null them out.

Consider, for example, the deformation of a monolithic circular mirror due to thermal loading. Figure 1-7, reproduced from [20], shows the normalized shape of the vertical deformation of the reflecting surface resulting from uniform thermal loading on one side. In order to cancel out this deformation, the truss structure supporting the mirror must apply a set of forces (or impose a set of displacements) onto the mirror such that the effect of that actuation is the negative of the shape in Figure 1-7.

The question of how many independent degrees of freedom are required to null out this deformation must begin with the question of what the effect of actuation actually looks like on the mirror surface. In large telescopes such as the Hale or the VLT, a plate-like reflector is supported at many points under its surface by

either active or passive devices that have some built-in compliance. The response of the mirror surface to an applied force (or an equivalent imposed displacement) can, therefore, be modeled by the response of a rigid plate on an elastic foundation. For small displacements, the analytical form of the deformation is well-known [29], and will be reproduced as follows: In two dimensions, the deformation $w(x, y)$ of a plate perpendicular to its surface in response to an applied force load is governed by the bi-harmonic equation:

$$\frac{\partial^4 w}{\partial x^4} + 2\frac{\partial^4 w}{\partial x^2 \partial y^2} + \frac{\partial^4 w}{\partial y^4} + \frac{kw}{D} = \frac{q}{D} \tag{1.1}$$

where k is the effective reaction force density of the support truss to vertical displacement, D is the flexural rigidity of the plate material, and q is the distribution of force applied perpendicular to the mirror surface. Note that if the actuation occurs as a displacement imposed between the compliant support and the mirror, Equation 1.1 requires renormalization by an appropriate spring rate, but the functional form of the solution remains.

If we assume that "infinite plate" plate boundary conditions approximately hold (an assumption to be justified momentarily), and q is a point load, then the solution to 1.1 is given by

$$w(r) = -\frac{(D/k)^{1/2}}{2\pi D}\text{kei}\left(r\left(\frac{k}{D}\right)^{1/4}\right)q \tag{1.2}$$

where kei $(\cdot)$ is the so-called Kelvin function, which is plotted in Figure 1-8. There are two immediate facts that should be apparent from both the plot and the analytical form. First, if the infinite boundary assumption holds, then there is no appreciable deformation at a distance

$$r > 4\left(\frac{D}{k}\right)^{1/4} \tag{1.3}$$

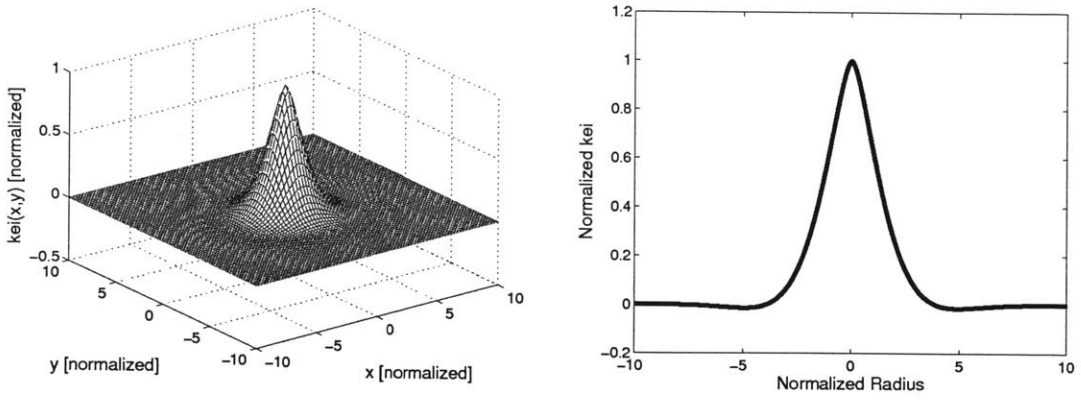

Figure 1-8: Kelvin Function kei(·) Plotted in Two Dimensions and In Cross-Section

away from the actuation point. Note that if the actuation point is sufficiently interior to the boundary (that is, much more than $4\left(\frac{D}{k}\right)^{1/4}$ distance units inside), then the infinite boundary condition holds, and Equation 1.2 indeed models the deformation of the mirror in response to a actuation at a point. The actual physical width of the response depends (as in a one-dimensional beam on an elastic foundation [29], [18]), on the ratio of the stiffness of the support k and the mirror plate flexural rigidity D. Specifically, the extent of the region of influence of a single actuator on the mirror surface shrinks with increased support stiffness relative to the mirror and expands with increased mirror rigidity relative to the supports. Given the necessarily low rigidity of thermally stable glass mirrors, this is one of the reasons that even all-passive mirror supports require many support points under the mirror surface.

The second fact, which answers the primary question of this section, is that the shape of the mirror response in Figure 1-8 does *not* match the shape of the thermal deformation in Figure 1-7. This point bears repeating: when the mirror support is stiff relative to the mirror surface itself, which *will* be the case with large mirrors, the thermal deformation associated with even a uniform temperature load *cannot* be

canceled out with a single actuator directly manipulating the surface of the mirror.

Thus, in order to cancel out such a deformation, either many independent continuous actuators must be placed under the surface of the mirror in sufficient proximity to allow for a smooth response from their collective action, or the interior of the support truss must be actuated in a specific way such that the top surface of the truss deforms into the negative of the thermal disturbance.

This latter approach may seem attractive from a control point of view because it requires fewer degrees of freedom. However, it will be the position of this Thesis that it is difficult to design, even if it is possible, and that it may not be robust to different disturbance conditions. This necessarily introduces the complication of requiring more independent degrees of freedom. The remainder of this document will be focused on finding truss and actuator geometries that allow for independent control of the displacements of many points on the top surface of the mirror support truss, where the actual number of degrees of freedom required will be determined by the relative stiffnesses of the mirror and support structure.

1.2 State of the Art in Theoretical Binary Mechatronics

This section will describe the mathematical peculiarities of binary-actuated mechanisms as they relate to various performance metrics one may use to characterize manipulator robots or optical systems. Implementation details of physical actuators are outside of the scope of this Thesis, and for the purposes of this discussion, idealized on/off force elements or bistable kinematic elements will be assumed to exist, and will be assumed to be within their operating envelope.

1.2.1 Workspace and Forward Kinematics

The first question to ask is, "what does the workspace look like?" The answer is simple. For a system with N binary actuators, there are exactly 2^N possible kinematic states the system can take. In certain instances, however, symmetries within the mechanism cause many of those 2^N possible kinematic states to overlap in end-effector position.

This idea is best illustrated graphically. Consider the serial chain binary manipulator in Figure 1-9, which consists of identical-length links with joints that can take on exactly two possible angles of identical magnitude but opposite sign.

Suppose that the mechanism is exactly 10 links in length. Figure 1-10 shows a point cloud of all 1024 ($= 2^{10}$) possible end effector locations achievable under the 1024 possible kinematic states of all 10 joints. Observe, however, that because all the links are of equal length and the joints are all identical, there exists a symmetry in many of the kinematic configurations. Figure 1-11 illustrates this symmetry in the outermost points of the end-effector workspace. There are exactly 56 distinct

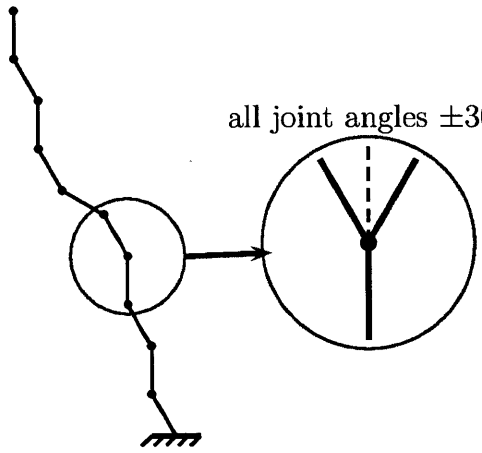

Figure 1-9: Simplified Serial Chain Binary Mechatronic Mechanism

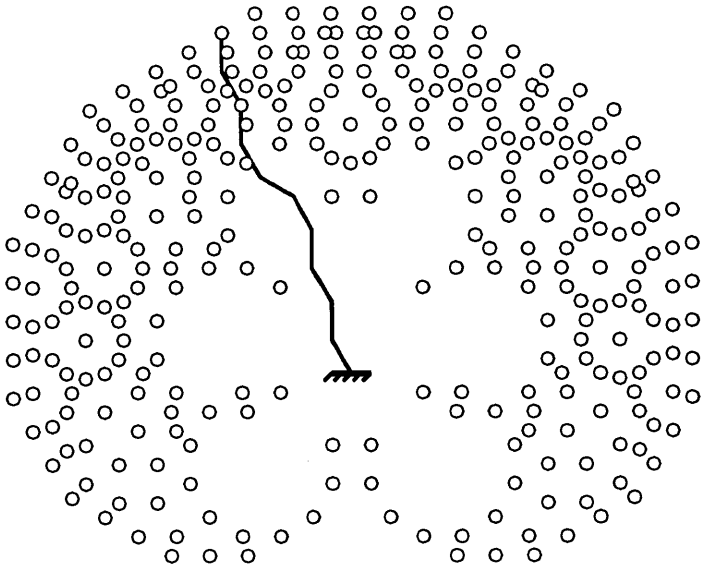

Figure 1-10: Complete Workspace of Simplified Serial Chain Mechanism

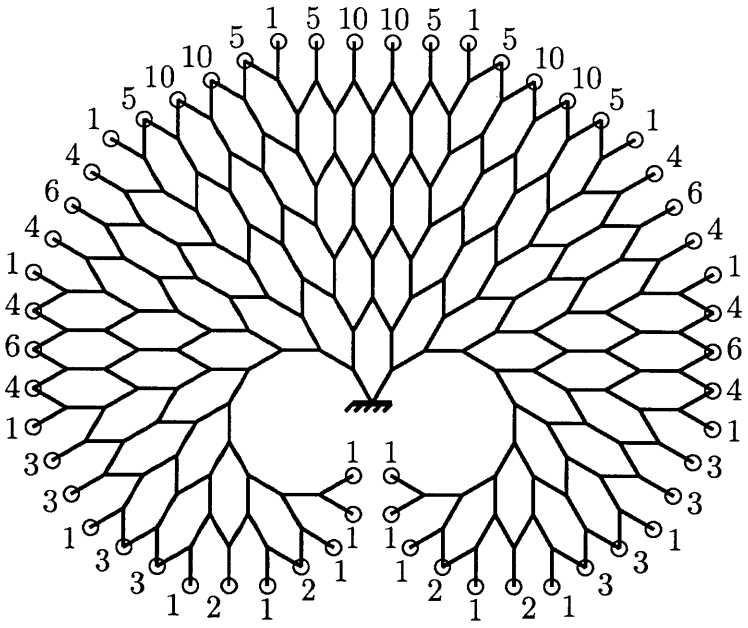

Figure 1-11: Degeneracy in the Workspace of the Simplified Serial Chain Mechanism

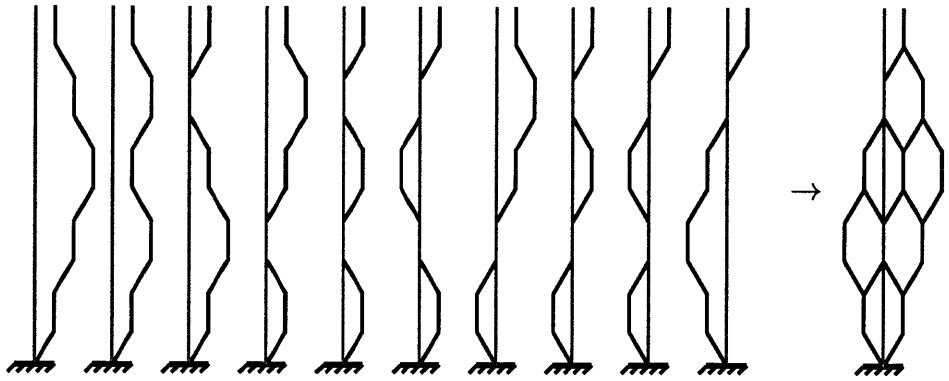

Figure 1-12: Detail of Degeneracy in the Workspace of the Simplified Serial Chain Mechanism. Ten Distinct Kinematic Configurations Are Degenerate to a Single Point.

points on the periphery of the the end-effector workspace, but they are visited by 198 distinct kinematic configurations of all the joints. While some of these end-effector points are visited by exactly one unique kinematic configuration, several have as high as a 10-fold degeneracy, as illustrated in Figure 1-12. Indeed, because the self-similar hexagonal tree structure for this example does not need to start at the zeroth node, but can be rooted at any link in such a mechanism, there are more degeneracies in the interior of the workspace. Overall, when all such symmetries are accounted for, the 1024 distinct kinematic configurations of this 10-link mechanism are degenerate to only 320 unique end-effector positions.

It is possible to take this overlapping phenomenon to its extreme, and design a 1-d.o.f. linear positioning mechanism by stacking N identical piston actuators in series. The overall length of the mechanism is the sum of the lengths of the individual pistons, but because all of the pistons are identical, the total length can only take N values, even though there are 2^N possible combinations of individual actuator lengths.

Depending on the philosophy of the design, this can be a desirable property. One of the original motivations of the research into binary mechatronics is the possibility of constructing "hyper-redundant" systems which can tolerate the loss of several binary actuators without a catastrophic performance penalty. In this case, the extreme symmetry of the previous example and the overlap illustrated in the serial manipulator are design goals rather than complications.

The alternate philosophy, which this Thesis will adopt and which will be formalized later, is that rather than being redundant, a design should not waste configurations. The justification for this philosophy is that redundancy and overlap are directly opposed to the goal of increased position resolution at the end effector. If there are only 2^N possible kinematic states for a fixed N, then redundancy in

any end-effector configuration comes directly at the expense of reachability of other possible positions. Indeed, in certain applications [7], the specification for a robot manipulator is given in terms of workspace resolution and workspace size, rather than redundancy on any given point in the workspace, and the design challenge is to produce a mechanism with a specified resolution or precision at the end-effector.

In order to achieve "greater reach" with a given number of binary actuators, designs do what is termed *breaking symmetry*, whereby the self-similar structures such as those of the example in Figure 1-11 are perturbed so that the overlap at the end-effector for different kinematic configurations is not total. In the case of the serial mechanism, variable geometry trusses which introduce complex nonlinear rotations are known to break the symmetry of hyper-redundant binary mechatronic manipulators to allow for a more uniform workspace density [3], [10], [11].

A particularly illustrative example of breaking symmetry was the design of a 2-d.o.f. medical imaging positioning stage by DeVita and Plante [8], [7], where a deliberate mechanical asymmetry was introduced into elastic elements of the 12-actuator mechanism shown in Figure 1-13 in order to spread the possible end-effector (x, y) coordinates more uniformly in the workspace.

In general, as the number of actuators increases, and their symmetry is appropriately broken, the discrete workspace of the binary mechatronic system approaches that of the continuously-actuated mechanism [27].

1.2.2 Complications in Inverse Kinematics

This section will describe issues of inverse kinematics that are particular to binary mechatronic systems with many actuators. The standard method of doing inverse kinematics for a redundant multi-link robot (or an overdetermined elastic system)

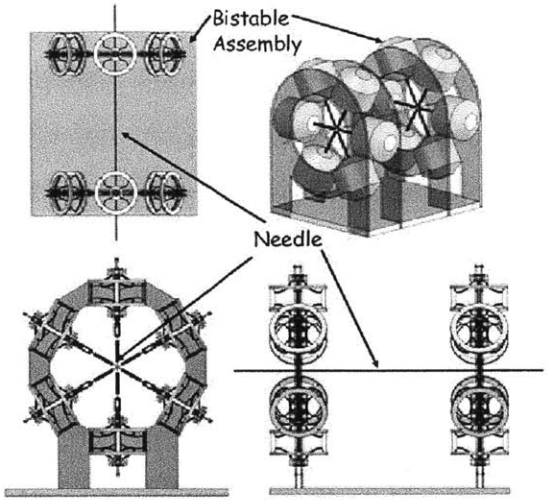

Figure 1-13: Two-D.O.F. Medical Imaging Positioning Stage with Asymmetric Elastic Elements Constructed by DeVita [8]

with continuous actuators consists of computing a (well-defined) kinematic Jacobian transformation to map from differential actuator perturbations and the corresponding differential end-effector positions. To first order, and neglecting dynamic terms, this can be written as

$$\Delta\vec{y} = \mathbf{J}\Delta\vec{u} \tag{1.4}$$

where $\mathbf{J}$ is the geometry-dependent kinematic transformation, which always exists and is well-defined, $\Delta\vec{y}$ is the scalar or vector perturbation in the end-effector position, and $\Delta\vec{u}$ is the continuous perturbation in the actuator effort.

Provided some desired end-effector trajectory $\vec{y}(t)$ is reachable by the robot, the corresponding control time-history required to achieve it can be computed by breaking the trajectory into distinct steps $\Delta\vec{y}$, and manipulating Equation 1.4 to yield

$$\Delta\vec{u} = \mathbf{J}^{+}\Delta\vec{y} \tag{1.5}$$

where $\mathbf{J}^+$ is the left pseudo-inverse of the Jacobian. It exists if the trajectory is reachable. Starting from a known initial end-effector state and corresponding known actuator configuration, Equation 1.5 can be used to compute the entire actuator time-history for the trajectory.

While the kinematic Jacobian exists for any well-defined mechanism, and Equation 1.5 can be computed for any nonsingular geometry, the differential actuator input $\Delta\vec{u}$ that is computed is assumed to be achievable for all values of $\mathbf{J}^+\Delta\vec{y}$. In binary mechatronics, all actuators are assumed to have only two discrete states, and the standard IK method results in an unimplementable actuator perturbation, making the method generally inapplicable to binary mechatronics.

Rather than being able to rely on the properties of mappings between continuous vector spaces, an explicit mapping from the continuous space of end-effector coordinates to the discrete set of 2^N possible actuator configurations must be computed, where the computation can either be through computer simulation of a calibrated system [21], or through exhaustive enumeration of all actuator configurations on the actual system [15]. Except in a few special cases, the computation time and data storage complexity of such an *exact* computation can be as high as $O(2^N)$, which quickly becomes intractable.

The next section will describe the state-of-the-art methods of both exact and approximate techniques for computing this map.

1.2.3 Brute Force Methods of Inverse Kinematics

For systems with a relatively small number of actuators, where the word "small" is an increasing function of available computing speed and memory (and therefore of cost and time), the exact computation of the map is tractable, as it is feasible

to compute (in simulation) the forward kinematics to all 2^N actuator configurations and to use that mapping and an appropriate rounding heuristic as a lookup table from continuous end-effector coordinates to the 2^N possible actuator configurations.

This approach was successfully used on the 12-actuator MRI positioning system constructed by DeVita and Plante [8], [7], where after experimental calibration with a small sample of measured end-effector positions and corresponding actuator configurations, the end-effector positions for the remaining set of actuator configurations were computed with a finite element simulation, yielding sufficient accuracy to be used as a lookup table [21].

This method was also by Lee in his exploratory work on applying binary mechatronics to optical systems to show that binary actuators embedded in a primary mirror support structure can be used to improve optical quality in large telescope systems subject to kinematic disturbances [14], and was demonstrated in the 13-actuator steering mirror constructed by Bilton to demonstrate feasibility [15].

At this point, it is instructive to ask why one may design a mechanism with more actuators? If a 12-actuator system with broken symmetry yields 4096 states that are sufficiently uniform to achieve required precision for medical imaging work, and the calibrated precomputed forward kinematics is both tractable and sufficiently precise, why would one want to design a system with more actuators?

The answer comes from the actuation requirements on large optical mirrors. As shown in Section 1.1.2, large mirrors require many support points. If a active control of these support points is required, then the number of independent degrees of actuation necessarily increases, and the dimensionality of the required workspace increases with the number of actuators. Instead of being confined to a plane, or a cube, as in the case of the coordinates of the end-effector of the serial link arms, the workspace is now spread over $\mathbb{R}^n$, where n is a very large number like 150, in the case of the

VLT mirror support control system.

The number of states we have at our disposal to distribute across our workspace must scale with the dimensionality of our workspace in order to maintain the same resolution of end-effector coordinates along any one dimension of our higher-dimensional space. If we are in a 1-dimensional workspace, our precision, or resolution, requirement can be stated in terms of "states per unit length", but in two dimensions, it is "states per unit area", in three, it is "states per unit volume", and in general it is "states per n-dimensional hypercube of specified n-dimensional volume. In general, the number of such volumes in the total workspace scales exponentially with the dimension n, and the number of discrete actuator configurations at our disposal must also scale exponentially, and correspondingly, the number of discrete actuators must scale linearly with the number of degrees of freedom.

1.2.4 Heuristic Search Methods of Inverse Kinematics

Given the pressure to increase the number of actuators in a binary mechatronic system, considerable research effort has gone into developing efficient heuristic searches that exploit structure in mechanism topology to compute tight approximate solutions to the inverse kinematics problem without requiring $O(2^N)$ computational time complexity. In the case of serial manipulators, the hierarchical structure of the actuators can be exploited to expedite the search.

Lees and Chirikjian presented a framework for synthesizing continuous curves from the base of the serial manipulator to the desired endpoint, and sequentially computing the configuration *for each level* of the manipulator that most closely causes the manipulator to hug the curve *at that level.* Because this optimization is performed only once at each step along the length of the curve, the total computa-

tional complexity is $O(N)$. Issues of kinematic reachability, constraints on the curve, and the proper relative weighting of "hugging error" between the manipulator and the curve at different distances from the base were addressed in the formulation for synthesizing the optimal curve and the optimal error weighting as a function of the curve [16].

Another method proposed reducing the search space by fixing the maximal number of bits allowed to change state during a motion. Recognizing that large motions require transitions of actuators closer to the base of the manipulator while smaller motions can be accomplished with transitions of bits closer to the tip, Lees and Chirikjian showed that it is possible to exploit a lexicographic sorting of actuators to reduce the search space down to several bit transitions and achieve good trajectory tracking in a serial manipulator [17]. This method was used for the basis of a genetic-algorithm search for the BRAID design by Sujan, Lichter, and Dubowsky [27].

The final "classical" approach to the inverse kinematics problem is defined in terms of a gradient-descent on spatial densities of end-effector states rather than combinatorial searches of bit strings.

For discrete serial mechanisms, one can define a quantity called the *workspace density* for a given volume of space from an initial set of coordinates for some link of the serial mechanism as the number of kinematic configurations of the entire mechanism starting from that link which place the end-effector in that volume. This can be thought of as the *probability* that there exists a manipulator configuration which places the end-effector in that volume of space [11]. It can be shown that the computation of this density for a serial mechanism can be done recursively via a convolution in the spatial domain, and that the computational complexity of this recursion and convolution is linear in the length of the mechanism (multiplied by the spatial resolution being considered) [10].

The algorithm proposed by Ebert-Uphoff and Chirikjian exploits this computational efficiency by formulating the heuristic search in terms of a maximizing at every link the *probability* of reaching the desired endpoint with the end-effector, where the probability is calculated as described above.

The drawback of these methods of inverse kinematics is that while they are computationally efficient, because they are approximate computations, they cannot *guarantee* both precision at the end-effector *and* a bound on computation time. More importantly, because they are optimized to exploit the hierarchical nature of serial link mechanisms, there is no clear path for extending them to parallel geometries inherent in the optical surface control problem.

1.2.5 Exact Constant-Time Methods

The last method to be discussed, and the central focus of the remainder of this Thesis, exploits the basic properties of the positional binary number system to design an actuator geometry where individual actuators correspond to binary bits in the numerical expansion of a target coordinate in one degree of freedom. This allows the computation of the binary input word to all the actuators by simply scaling the desired position by an appropriate constant, expressing the result in binary notation, and directly inputting those bits into the actuators.

In the binary positional number system, a binary word $B_N B_{N-1} ... B_2 B_1$ has the numerical value $\sum_{i=1}^{N} 2^i \times B_i$ where $B_i \in \{0, 1\}$. Observe that each bit B_i represents a magnitude exactly twice that of its less significant neighbor B_{i-1}, and this *geometric decay* holds for the length of the entire binary word. By the basic properties of binary notation, the entire word is capable of exactly representing all the integers ranging from 0 to $2^N - 1$ with a resolution equal to the least-significant-bit (LSB),

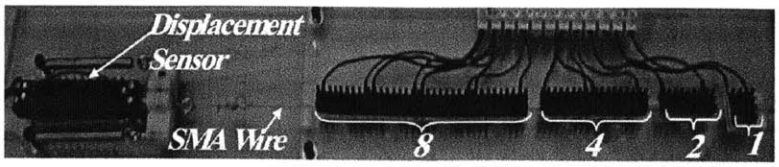

Figure 1-14: Single-Axis Binary Length Actuator Built by Cho and Asada to Exploit Constant-Time Exact Inverse Kinematics [4].

corresponding to the magnitude represented by B_1.

Because computing the binary expansion of a scaled value is trivially easy and extremely fast (all computers natively represent all quantities as binary numbers and have dedicated hardware for fast multiplication and rounding of binary quantities), it is compelling to search for an actuator design where the difference between the ON and OFF positions of individual actuators also follows geometric decay, resulting in a set of actuators whose state corresponds to the bits of the binary expansion of a scaled and rounded coordinate of the degree of freedom being actuated.

One of the first designs with this property was an 8-bit hydraulic actuator constructed by Delmege and Tremblay in 1965 for use in aircraft control surfaces [6]. This actuator consisted of a series of eight hydraulic pistons, each of which had exactly twice the travel of the previous one.

Cho and Asada constructed a similar mechanism using expansion and contraction of precise lengths shape-memory-alloy (SMA) wires for control of a robotic hand [4]. The design exploits the fact that the total strain of an SMA segment under thermal load is proportional to the length of the segment. Using an actuator consisting of several segments of normalized length 1,2,4, and 8, as shown in Figure 1-14, 16 equally-spaced end-effector states, with a resolution equal to the LSB were achieved.

While this approach is appealing because of the simplicity of the inverse kinematics, it suffers a drawback in that the dynamic range of the assembly and manufactur-

ing process for this design is required to be as large as the dynamic range between the resolution and maximum extent of the mechanism. Indeed, in the case of the digital hydraulic actuator, the machining tolerance on the cylinder stops is required to be as tight as the LSB piston. The remainder of this Thesis introduce a design methodology which exploits *mechanism elasticity* to give the same geometric decay of actuator *influence* magnitudes (allowing constant-time exact inverse kinematics), but that requires a low dynamic range of actuator magnitudes themselves.

1.3 Outline of the Original Contribution

Having established the context for surface figure correction in large optical systems such as solar concentrators, large radar dishes, and especially large optical telescopes, as well as the challenges in binary mechatronic design, the remainder of this Thesis will take a more theoretical approach to defining the specific requirements for applying binary mechatronics to a general elastic, multi-d.o.f mechanism.

Chapter 2 will establish some mathematical preliminaries related to the influence of small-stroke binary actuators on large compliant mechanisms. An analogy will be constructed between the kinematics of massively parallel binary actuated systems and the theory of probability distributions of many independent random variables. A tight lower bound will be determined on the minimum number of binary actuators required to control a given number of *independent* degrees of freedom within a specified dynamic range. Additionally, it will be shown that if an actuator design exists that meets this lower bound, then the inverse kinematics for that design will necessarily be trivially easy, and deterministically computable in constant time.

Chapter 3 will then demonstrate that there exist compliant mechanisms constructible from basic elements such as springs, cables, and piston actuators, that

exploit elastic averaging [24] to achieve the optimality condition derived in Chapter 2 for a single degree of freedom. Finally, Chapter 4 will extend that design philosophy to develop a mechanism to control multiple independent degrees of freedom on the top surface of a truss structure in a way amenable to active surface figure control in optical systems.

As will be shown in Chapter 4, any practical implementation of binary mechatronic control of a deformable mirror surface will require a large support structure with many thousands of distinct elements, and (depending on the size of the mirror) possibly hundreds of actuators. For this reason, this Thesis will be confined purely to analytical proofs and numerical simulations rather than experimental validation of the mechanisms proposed herein.

Chapter 2

Mathematical Preliminaries

Previous work on binary mechatronic mechanism falls into two categories: mechanisms where rotation-induced nonlinearities limit the utility of analysis in terms of individual actuator influences on the entire system, and mechanisms specifically designed to exploit superposition to greatly simplify the inverse kinematics by allowing very powerful *global* statements about all 2^N discrete mechanism configurations to be made in terms of the geometries of only the N individual actuators. Chirikjian, Ebert-Uphoff, and Lees's serial manipulator mechanisms and Sujan, Lichter and Dubowsky's BRAID concept fall in the former category. Indeed, a cursory inspection of the workspace of the representative mechanism shown in Figure 1-11 reveals that the binary joint closest to the end-effector of such a device can have an influence on the x-coordinate of the end-effector that varies anywhere from a maximum when the end-effector is directly above the base of the mechanism to zero when the arm is bent left or right. Cho and Asada's SMA actuator, and Delmage and Tremblay's binary hydraulic actuator, on the other hand, fall into the latter category, where the displacement contributions of individual segments sum arithmetically to the dis-

placement of the end-effector, greatly simplifying the analysis and control of the mechanism. Indeed, the control algorithm for these latter mechanisms is *optimally fast*, as it requires only a scale and truncate operation on the numerical value of the desired end-effector coordinate.

The purpose of this Thesis is to explore the applicability of binary mechatronics to actual, deployable, optical systems. For this purpose, optimality in terms of mechanism accuracy, resolution, as well as control algorithm execution time is required. This chapter will lay down the mathematical framework that is necessary to reason about these requirements and the designs that meet them.

First, Section 2.1 will establish that there exist real compliant mechanisms with binary actuation for which it is appropriate to conduct the analysis of mechanism kinematics in terms of influence functions of individual binary actuators. Section 2.2 will derive the optimal distribution of discrete end-effector positions that a binary mechatronic mechanism should achieve to maximize accuracy with a finite number of actuators. Section 2.3 will then build a rigorous analogy between the mathematics of sums of independent discrete random variables and the kinematics of binary mechatronic systems *where superposition holds.* Lastly, Section 2.4 will use that analogy to develop a recipe for constructing binary mechatronic systems that meet the accuracy-optimal end-effector distribution requirement derived in Section 2.2 *and* as a consequence of that optimality constraint, will also be controllable by the trivially simple inverse kinematics seen in Cho and Asada's and Delmage and Tremblay's designs.

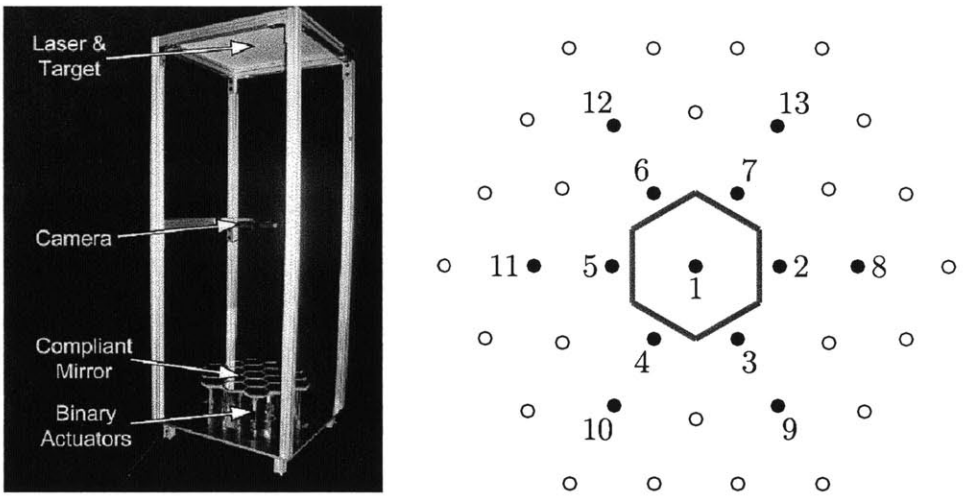

Figure 2-1: Left: photograph of 13-actuator experimental system constructed by Bilton [15]. Right: Actuator Layout. Labeled filled circles denote actuator locations, open circles denote compliant support locations, hexagonal outline denotes boundaries of center mirror measured in experiment.

2.1 Linearity and Superposition in Elastic Binary Mechatronic Systems

While no real physical system is ever truly linear, even highly coupled, over-constrained binary actuated mechanisms are known to have linear operating regimes. This section will quote, and elaborate on, results obtained by Bilton and Lee [15], with the purpose of specifying exactly the extent of the linearity required for the analysis in the remainder of this chapter to hold, and demonstrating that mechanisms can be constructed to meet these requirements.

Figure 2-1 shows the compliant binary mechatronic steering mirror mechanism constructed by Bilton to validate the numerical intuition developed by Lee in [14]. The kinematics of this mechanism are over-constrained, and elastic averaging holds

[24]. It is therefore appropriate to consider Taylor approximation to the functional form of the displacement or rotation of any point on the deformable surface of the mechanism (for instance, the tilt in the x-direction of the center mirror) as a function of actuator inputs. The question is, is a first-order approximation of the form

$$\Delta\theta_x = \sum_{i=1}^{13} w_i \Delta x_i + \text{h.o.t.} \tag{2.1}$$

sufficient to capture the dominant behavior of the center mirror in this mechanism?

To answer this question, Bilton and Lee measured the deflection of the center mirror along the x direction for all 8192 ($= 2^{13}$) configurations of binary actuators in the mechanism. This list was sorted, and for each of the 13 actuators, the difference was computed between the 4096 instances when that actuator was ON and the 4096 instances when that actuator was OFF. If superposition were exactly true, then these differences would be exactly identical in magnitude, but because the mechanism was not perfectly linear, there was an approximately Gaussian spread in these influences, which is plotted for selected actuators in Figure 2-2.

The question of whether the assumption of linearity holds rests on the ratio of the size of this spread in tilts to the magnitude of the mean tilt induced by a given actuator. If, for example, the combined nonlinearity error from all the actuators is smaller than the finest mean tilt associated with some finest actuator, then the linearity assumption would not be violated to within the tolerance of the overall actuator configuration. In the case of Bilton and Lee's mechanism, the size of the nonlinearity error for actuators 2-7 is smaller than their mean influence magnitudes, and in this mechanism, linearity can be safely assumed to hold for the inner ring of actuators.

In his exploratory work on applying binary mechatronics to multi-d.o.f. highly-

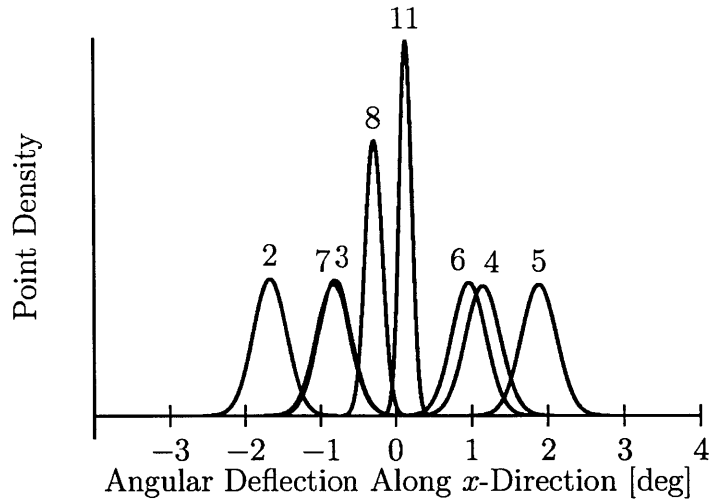

Figure 2-2: Variance of Actuator Influence in Bilton's Experiment. Gaussian fits of distribution of influences of selected actuators on mirror deflection in mechanism x-direction.

coupled compliant mechanisms, Lee showed [14] that the nonlinearity error decreases rapidly with smaller inputs, suggesting that the "signal-to-noise" in the linear region can be increased, and the size of the linear region itself can expand with careful design. This demonstrates that in real mechanisms, superposition can potentially be exploited.

2.2 The Optimal End-Effector Position Density

Suppose we wish to design a binary mechatronic actuator that moves along a given degree of freedom (say, along the x-axis) within a specified range (say, the interval $[0, 1]$). If the number of actuators we have at our disposal is some fixed number N (meaning we have 2^N possible actuator configurations, corresponding to at most 2^N possible positions along the x-axis), what is *optimal* distribution of those 2^N possible

positions along the x-axis on the interval $[0, 1]$?

2.2.1 The Optimality Metric

We begin to answer this question by stating exactly which optimality metric is important. For a position actuator moving along a single degree of freedom, it is natural to define performance in terms of minimizing the error between some specified target position and the best possible actual position achievable by the actuator in response to that command.

There is an uncountable infinity of possible continuous target positions, but only a finite number of possible discrete actuator positions in the interval of interest. It is therefore natural to define the error metric probabilistically as the total *expectation* of the error over the entire range of motion of the actuator, in the manner of [8]. Symbolically, if $\mathbb{S}$ denotes the set of 2^N available discrete positions, the error metric (along the x-axis) can be written as

$$\mathcal{E} = E_X \left[\min_{S \in \mathbb{S}} |X - S| \right] \tag{2.2}$$

where X is a *continuous* random variable which represents the unknown possible target position and takes values in the interval $[0, 1]$ along the x-axis. Because the time-history of the required target position is not known a priori in the design phase, the probability density of X must be selected to have the least a priori information, or, equivalently, the maximal entropy. The distribution that has this property is the uniform continuous random variable [5].

The optimality requirement is then to select a set $\mathbb{S}$ of 2^N end-effector positions such that $\mathbb{S} \subset [0, 1]$ which minimizes the expectation $\mathcal{E}$ defined in 2.2 when $X \sim \mathcal{U}(0, 1)$.

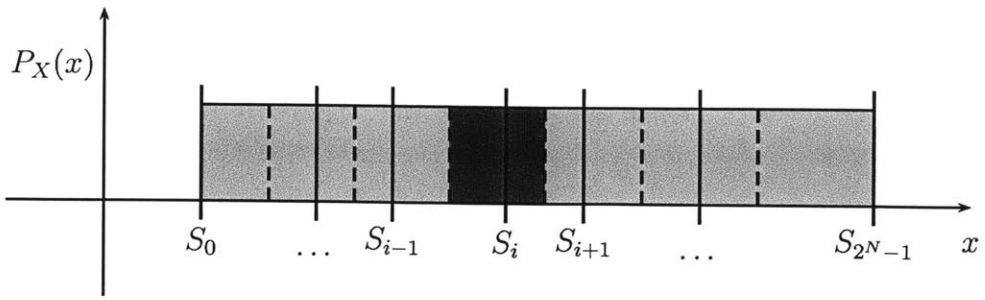

Figure 2-3: Probabilistic Error Metric. Dark shaded area represents $\mathcal{E}_i$

To minimize $\mathcal{E}$, consider Figure 2-3, which plots the distribution of X and the possible discrete actuator positions S_0 through S_{2^N-1} along the unit interval. Suppose we sort the end-effector positions left-to-right, and let S_{i-1}, S_i, and S_{i+1} be in the interior of the interval. Observe that for $x \in \left(\frac{S_{i-1}+S_i}{2}, \frac{S_i+S_{i+1}}{2}\right)$ (shaded dark in the figure), the expectation in 2.2 takes the form $E_X(|X - S_i|)$, where i refers to the same end-effector position in the entirety of that subinterval. This implies that we can partition the expectation in Equation 2.2 as follows.

Define the symbol $\delta_i = S_i - S_{i-1}$, then write the portion of the expectation in the subinterval $x \in \left(\frac{S_{i-1}+S_i}{2}, \frac{S_i+S_{i+1}}{2}\right)$ as

$$\mathcal{E}_i = \int_{-\delta_i/2}^{0} (0 - x) \cdot 1 dx + \int_{0}^{+\delta_{i+1}/2} (x - 0) \cdot 1 dx \tag{2.3}$$

where the first term comes from the error when X is to the left of S_i and closer to S_i than to S_{i-1}, the second term comes from the error when X is to the right of S_i and closer to S_i than to S_{i+1}, and the explicitly written factor of unity comes from fact that the random variable X is uniformly distributed on the unit interval and thus has constant unit density. Observe that by the disjointness of the intervals (S_i, S_{i+1}), the total expectation $\mathcal{E}$ over the whole interval will be identical to the sum of the

individual expectations $\mathcal{E}_i$ as defined by 2.3.

Evaluating the integral in 2.3, we find that the contribution of the i^{th} discrete actuator state to the total error metric is given by $\mathcal{E}_i = 1/8\left(\delta_i^2 + \delta_{i+1}^2\right)$. Summing over contributions of all the discrete states, we then find that the error metric can be written as

$$\mathcal{E} = \sum \mathcal{E}_i = c \sum \delta_i^2 \tag{2.4}$$

for some geometry constant c, which remains fixed over the all i's in the case of a uniformly distributed X.

2.2.2 The Optimality of the Uniform Density

Given this formulation of the error metric in terms of the separation distances δ_i between the 2^N possible end-effector positions, we would like to find a set of separations that minimize the error metric. We do so by a variational argument as follows.

Observe first that if our end-effector positions $\mathbb{S}$ span the unit interval, and we make the assumption that the first position occurs at $x = 0$ and the last at $x = 1$, we can write that

$$\sum_{i=1}^{2^N-1} \delta_i - 1 = 0 \tag{2.5}$$

Recalling the objective function to minimize in Equation 2.4, we form the Lagrangian:

$$L(\vec{\delta}, \lambda) = c \sum \delta_i^2 + \lambda \left(\sum \delta_i - 1 \right) \tag{2.6}$$

where $\vec{\delta} = (\delta_1, ...\delta_{2^N-1})$ is the vector of separation distances between the possible end-effector positions.

To find the optimal $\vec{\delta}$, consider the i^{th} term in the derivative of the Lagrangian

with respect to $\vec{\delta}$:

$$\frac{dL}{d\delta_i} = 2c\delta_i + \lambda \cdot 1 = 0 \tag{2.7}$$

This holds for all i, and implies that $\forall i, \delta_i = -\lambda/2c$, which is to say that at an extremum of $\mathcal{E}$, all the end-effector positions are spaced equally over the unit interval. Note that this agrees with the intuition from lower dimensions that the way to minimize the sum-squared of a number of terms whose sum is fixed is by setting all the terms equal.

Thus the optimal distribution in terms of expected squared-error for a discrete set of end-effector positions, given a uniform distribution of possible target positions, is a uniform distribution of discrete end-effector positions, that is to say a distribution of positions spaced apart by equal intervals. This result is intuitively satisfying, both because of its simplicity, and because it lends itself quite readily to the exact constant-time inverse kinematics, as will be demonstrated in the remainder of this chapter.

2.3 The Equivalence of Probability Theory and Linearized Discrete Actuation

This section will develop a strong analogy between the theory of sums of independent discrete random variables and the kinematics of binary mechatronic systems where the position displacement of some point on the mechanism is given by a (weighted) linear sum of states of all the binary actuators in the mechanism. The purpose of building this analogy is to harness well-known results from the theory of probability distributions in order to construct the optimal (uniform) end-effector position distributions from sums of influences of individual binary actuators.

We begin by considering an abstract binary actuated mechanism composed of N actuators and one end-effector measurement point, whose discrete displacement s along the the x-axis in response to changes in actuator states can be written as

$$s = \sum_{i=1}^{N} w_i b_i \tag{2.8}$$

where w_i are the weighting factors, or *influence magnitudes* of the individual actuators and b_i are the binary states of the actuators, taking the values 0 or 1. Note that Cho and Asada's SMA-based muscle actuator, where $w = (1, 2, 4, 8)$ by design, is an example of such a system.

Consider now the exhaustive enumeration of the possible configurations of the set of N binary actuators and their respective end-effector displacements. This exhaustive enumeration contains exactly 2^N elements, and can *define a probability distribution* for a set of Bernoulli random variables B_i where each B_i takes on the values of either 0 or w_i, corresponding to the *influence* of the i^{th} binary actuator on the displacement of the end-effector measurement point.

Furthermore, this exhaustive enumeration also defines a set $\mathbb{S}$ of 2^N end-effector coordinates $\{s\}$, which can be used to define a discrete random variable S that takes on up to 2^N possible values given by the unique values of s in $\mathbb{S}$, and whose probability mass function (pmf) is defined by the number of times each of those values of s appears in the exhaustive enumeration.

For example, if we have a mechanism with two actuators with equal weighting factors of 1, such that $s = b_2 + b_1$. Then the exhaustive enumeration of the possible states of b_2 and b_1 has four elements and generates three unique values of s, shown in Table 2.1.

We then define the random variable S by the pmf shown in Figure 2-4, which

Table 2.1: Exhaustive Enumeration of End-Effector Position With Two Actuators

b_2	+	b_1	=	s
0		0		0
0		1		1
1		0		1
1		1		2

consists of the unique values of s generated in the exhaustive enumeration, each with a probability proportional to the frequency that those unique values are seen in the enumeration.

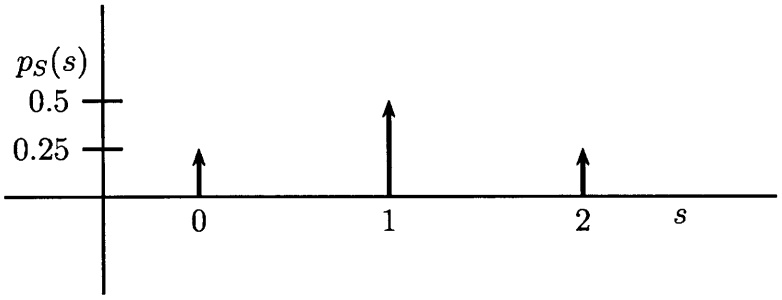

Figure 2-4: PMF for S Defined by Exhaustive Enumeration of s With Two Actuators

Observe that in our definition of B_i and S, we have made no new statements about the kinematics of the mechanism. All we have done in Table 2.1 is created an exhaustive enumeration of both sides of Equation 2.8 and defined new random variables from the columns of the enumeration while preserving the kinematic relation 2.8 in all the rows. This implies that we can rewrite the deterministic equation probabilistically as

$$S = \sum_{i=1}^{N} B_i \tag{2.9}$$

What is left to show is that the random variable S (whose pmf corresponds to

the distribution of end-effector positions) is, in fact, a sum of *independent* Bernoulli random variables.

Claim 2.1. *In the joint distribution of actuator bits defined by the exhaustive enumeration of their possible configurations, each B_i is independent.*

Proof. The proof is by induction. Consider the base case of two actuators, denoted B_2 and B_1. Table 2.2 enumerates the possible states of B_2 and B_1.

Table 2.2: Exhaustive Enumeration of Two Actuator Case

B_2	B_1	Joint Probability
0	0	1/4
0	1	1/4
1	0	1/4
1	1	1/4

Recall from the theory of probability that $P(B_2|B_1) = \frac{P(B_2 \cap B_1)}{P(B_1)}$, where the numerator is the joint probability. Recall also that the definition of independence is given by $P(B_2|B_1) = P(B_2)$.

By inspection of the table, we can observe that the four conditional probabilities for B_2 are all $P(B_2 = 0|B_1 = 0) = P(B_2 = 0|B_1 = 1) = P(B_2 = 1|B_1 = 0) = P(B_2 = 1|B_1 = 1) = 1/2$. We can also observe that cumulatively, $P(B_2 = 0) = 2/4 = 1/2$ and $P(B_2 = 1) = 2/4 = 1/2$. Thus, for this base case the conditional and unconditional probabilities are identically equal, and the two actuator random variables are independent.

We now proceed to prove the inductive step. Suppose that the joint distribution defined by the exhaustive enumeration of N binary actuator states has the property that all the N individual actuator state distributions are independent. We would

like to demonstrate that the joint distribution of $N+1$ actuator states defined by the exhaustive enumeration obtained after appending the $N+1^{th}$ actuator also has the property that all $N+1$ actuator distributions are independent. Symbolically, we would like to show that

$$P(B_{N+1}|B_N...B_1) = P(B_{N+1}) \tag{2.10}$$

Consider the expansion that occurs to the exhaustive enumeration of the binary random variables $B_N...B_1$ with the addition of the binary random variable B_{N+1}:

$$\begin{array}{|cccc|}\hline 0 & 0 & \ldots & 0 \\ \vdots & \vdots & \vdots & \vdots \\ \hline B_N & B_{N-1} & \ldots & B_1 \\ \hline \vdots & \vdots & \vdots & \vdots \\ 1 & 1 & \ldots & 1 \\ \hline \end{array} \longrightarrow \begin{array}{|c|cccc|}\hline 0 & 0 & 0 & \ldots & 0 \\ 0 & \vdots & \vdots & \vdots & \vdots \\ \hline 0 & B_N & B_{N-1} & \ldots & B_1 \\ \hline 0 & \vdots & \vdots & \vdots & \vdots \\ 0 & 1 & 1 & \ldots & 1 \\ \hline 1 & 0 & 0 & \ldots & 0 \\ 1 & \vdots & \vdots & \vdots & \vdots \\ \hline 1 & B_N & B_{N-1} & \ldots & B_1 \\ \hline 1 & \vdots & \vdots & \vdots & \vdots \\ 1 & 1 & 1 & \ldots & 1 \\ \hline \end{array} \tag{2.11}$$

Observe that any unique string $B_N...B_1$ appears exactly once in the enumeration of actuator bits 1 to N, and exactly twice in the enumeration of 1 to $N+1$, shown by the boxed rows the right-hand side of Equation 2.11. We can then write that for any such string, $P(B_{N+1} = 0|B_N..B_1) = 1/2$, and $P(B_{N+1} = 1|B_N..B_1) = 1/2$, since the string $B_N...B_1$ is appears exactly twice in the right-hand enumeration, once with $B_{N+1} = 0$ and once with $B_{N+1} = 1$. We then observe that in the enumeration, the

unconditioned probabilities of B_{N+1} are also exactly $1/2$, because by construction, when we append B_{N+1} to the enumeration, we transcribe the full enumeration of $B_N...B_1$ once with $B_{N+1} = 0$ and again with $B_{N+1} = 1$, resulting in exactly as many zeros as ones. Thus, equation 2.10 is shown to hold and the proof is complete. □

Having established that the joint distribution of the random variables $B_1...B_N$, defined by the exhaustive enumeration of the possible states of all N binary actuators, is independent, we re-interpret Equation 2.9 as saying that the *spatial density* of all 2^N end-effector positions in an linear N-actuator binary mechatronic system is given by the pmf of the sum of N independent Bernoulli random variables, each with parameter $p = 0.5$ and taking on the values of either 0 or the influence of that actuator on the displacement of the end-effector position. In the next section, we will use this fact to show how to construct a binary mechatronic system with the optimal uniform end-effector position distribution.

2.4 Constructing a Uniform Density

The theory of independent random variables is well developed, and has many powerful tools for analyzing the distribution of the sums of independent random variables. In particular, it is known that if two random variables B_1 and B_2 are independent and have pmf's given by $p_1(\cdot)$ and $p_2(\cdot)$, then the pmf $p_S(\cdot)$ of the random variable defined by the sum of B_1 and B_2 is given by the convolution of p_1 and p_2 [13].

The following graphical proof will review how to construct a discrete uniform random variable by summing independent Bernoulli random variables. The idea is that a uniformly distributed binary integer can be constructed by independently generating the bits from independent Bernoulli random variables.

Consider a Bernoulli random variable B_1 which takes on the values 0 and 1 with equal probability and an independent B_2 which takes on the values 0 and 2 with equal probability. Figure 2-5 demonstrates that the convolution of those two pmfs results in a uniform random variable.

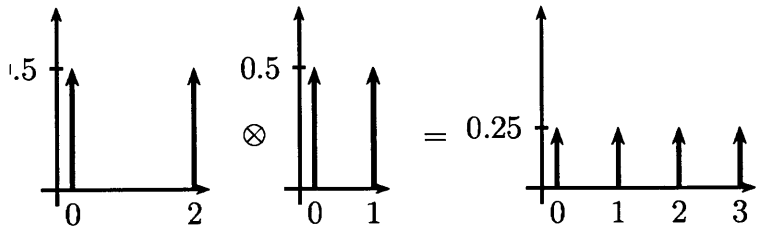

Figure 2-5: Convolution of PMFs of Two Bernoulli Random Variables Yields Discrete Uniform PMF

This suggests that if convolve together a series of uniform ($p = 0.5$) Bernoulli pmfs with widths that keep doubling (or equivalently, halving, that is *decaying ge-*

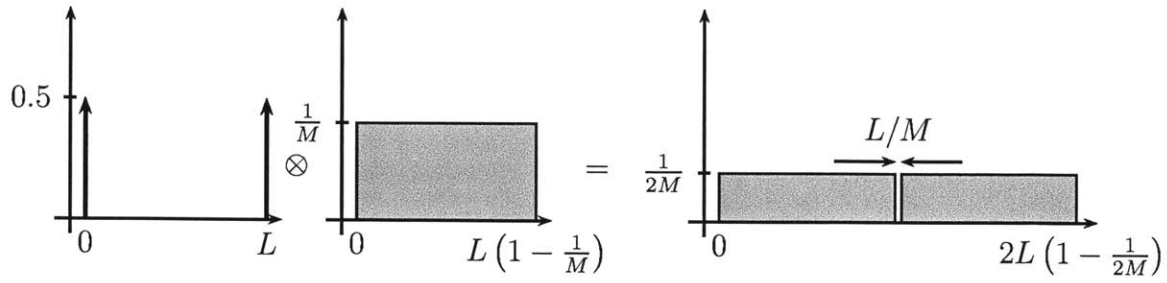

Figure 2-6: PMF Resulting from Appending the $N + 1^{th}$ Random Variable to Sum of N Random Variables

ometrically with decay factor 2), we will get a discrete uniform pmf over uniformly spaced values. Figure 2-6 demonstrates this graphically. The gray block represents a discrete uniform pmf over M $(= 2^N)$ *uniformly spaced* values between 0 and $L(1 - 1/M)$. Specifically, the spacing is exactly L/M. If we convolve that pmf with a uniform Bernoulli pmf over the values $(0, L)$, this has the effect of stacking two gray blocks adjacent to each other (and halving their height). Observe that the spacing between the last value of the left block and the first value of the right block must be $L - L(1 - 1/M) = L/M$, implying that *all* $2M$ $(= 2^{N+1})$ values are uniformly spaced, as required.

Observe that the geometric decay of actuator influences required to achieve the optimal discrete end-effector position density is exactly equivalent to equating individual actuator states to individual bits in the binary numerical expansion of the end-effector coordinate. This is exactly the design philosophy adopted by Delmage and Tremblay and Cho and Asada in their designs.

In summary, this chapter has shown that the optimal distribution of end-effector positions for a discrete mechatronic system with a required range of motion over some interval along a single dimension is the discrete uniform distribution. An analogy

was developed between the theory of distributions of sums of independent Bernoulli random variables and the distribution of the end-effector positions resulting from a linear superposition of many actuator influences. This analogy was used to describe a method by which a discrete uniform distribution can be constructed from sums of Bernoulli random variables whose magnitudes decay geometrically with a factor of 2. This provides a design target for binary mechatronic systems. Specifically, if the influences of the binary actuators on the displacement of a particular measurement point can be made to have geometric decay with a decay factor of 2, then a uniform density of mechanism positions can be achieved for that measurement point. Because the construction of this accuracy-optimal density leads naturally to actuator configurations with optimally fast inverse kinematics, searching for mechanisms where such a design is possible is a strong imperative. The remainder of this Thesis will explore designs for just such mechanisms.

Chapter 3

Existence of Elastic Mechanisms With Optimal Kinematics

Chapter 2 established that the optimal distribution of discrete end-effector positions in terms of accuracy is the uniform distribution, and that binary actuated mechanisms subject to linear superposition of actuator influences lend themselves naturally to achieving such distributions, provided that geometric decay of actuator influence magnitudes holds. Cho and Asada's SMA actuator and Delmage and Tremblay's binary hydraulic actuator designs achieve these simultaneous superposition and geometric decay requirements by using a series combination of displacement actuators whose strokes add, and whose lengths (strokes) decay geometrically. While both of these designs meet the optimality criteria formalized in Chapter 2, they suffer the drawback of requiring a high dynamic range in the absolute accuracy of their manufacturing process, stemming naturally from the large dynamic range in the lengths of the actuators corresponding to different bits. This Chapter will establish the existence of mechanisms which exploit *elasticity* to achieve linearity and geometric decay

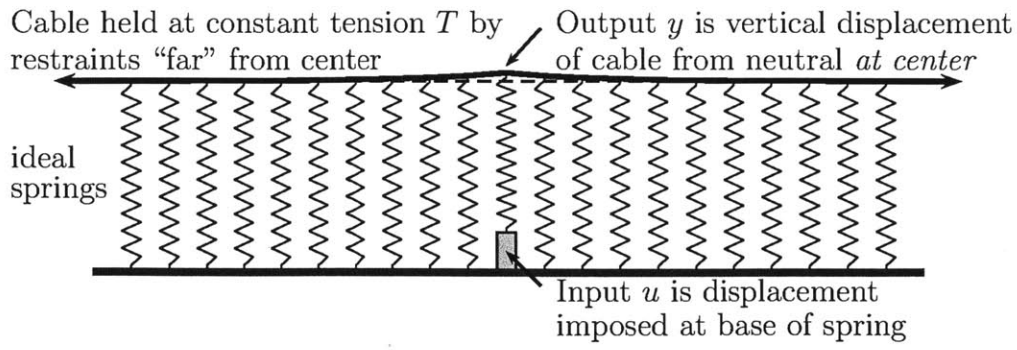

Figure 3-1: Center of the Taught Cable Mechanism

of influence magnitude for actuators of *constant magnitude.*

Consider an idealized cable held at constant tension, supported from below by ideal springs constrained to only the vertical degree of freedom. Input into this mechanism is introduced as an imposed vertical displacement at base of the springs, and the output is measured as the vertical displacement at a single point on the cable from its neutral position above the central spring.

It will be stated outright that this mechanism is impossible to implement in any practical sense for some very obvious reasons, but the statics of this mechanism have the important property that the influence of a kinematic displacement imposed into the base of a spring on the height of the cable above the *central* spring decays *geometrically* with the distance of the imposed displacement from the central spring.

The remainder of this chapter is organized as follows. First, Section 3.1 will derive the statics of this idealized mechanism and show that for small input magnitudes, the first order approximation $\mathbf{K}\vec{y} = \vec{u}$ appropriately describes the kinematics of the mechanism. Then, Section 3.2 will analytically derive the *influence matrix* $\mathbf{K^{-1}}$ [18], which will be used to demonstrate geometric decay of actuator influence on the center with increasing distance away from the center. Finally, Section 3.3 will

extend the analysis to other elastic mechanisms that transform *near*-constant magnitude actuators into exactly geometrically-decaying influences on the displacement of certain parts of the mechanism.

3.1 Stiffness Matrix for the Taught Cable Supported by Springs

In the derivation that follows, the force of gravity will be neglected, and use of the terms "vertical" and "horizontal" will refer only to directions on the page. This omission can be justified by the assumption that the stiffnesses of the cables and springs involved are significantly greater than their weight, or that the system exists in a horizontal plane perpendicular to gravity. Additionally, the assumption will be made that the cable is straight between adjacent spring points and admits sharp corners at the spring points.

We begin by considering a point in the interior of the cable and writing the static balance conditions for that point. Figure 3-2 shows schematically the forces acting on the point where the i^{th} spring meets the cable. There are three forces acting on the center of the cable. The first force results from the compression (or extension) of the spring between the equilibrium cable height at the center of the figure and the imposed vertical displacement at the base of the spring given by u_i. Assuming the relaxed spring length is y_0 and the spring rate is k_i, this force is given by

$$F_{\text{spring}} = k_i \left(u_i + y_0 - (y_i) \right) \tag{3.1}$$

The other two forces come from the vertical component of the tension in the cable on either side of the i^{th} point. Suppose that the tension in the cable is approximately

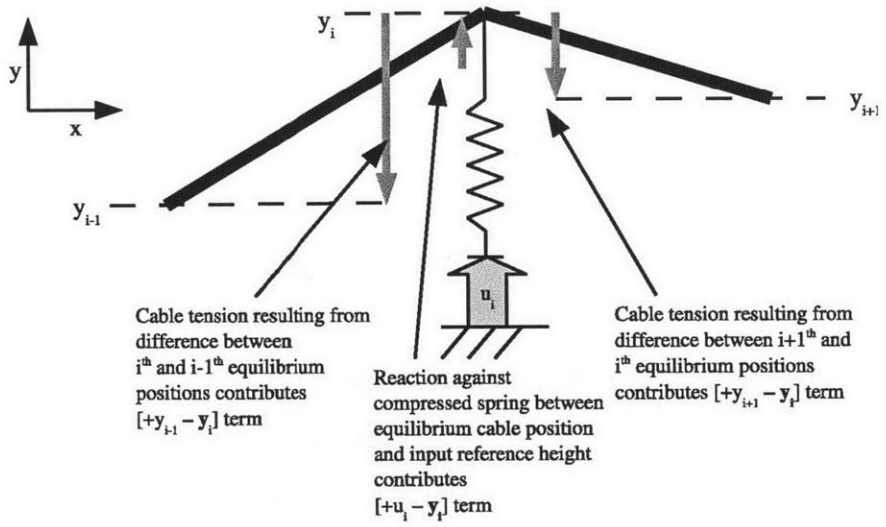

Figure 3-2: Taught Cable Force Balance Diagram

constant through the length of the cable and is denoted by T. Then the magnitude of the force coming from the left and right sides in Figure 3-2 can be written as

$$F_{\text{left}} = T\sin(x_{i-1}, y_{i-1}, x_i, y_i) \tag{3.2}$$

$$F_{\text{right}} = T\sin(x_{i+1}, y_{i+1}, x_i, y_i) \tag{3.3}$$

where the symbol $T\sin(x, y, x', y')$ denotes the vertical component of the tension in the cable running straight between the two coordinates. If we make the approximation that the displacement in the vertical direction are small relative to the spacing of the springs, such that $\sin\theta \approx \tan\theta$, then the $\sin(....)$ term can be written as

$$\sin(x, y, x', y') \approx \frac{y' - y}{x' - x} \tag{3.4}$$

Combining everything together, the balance of forces at the top of the i^{th} spring is given by

$$0 = -k_i\left(y_i - (y_0 + u_i)\right) + T\frac{y_{i-1} - y_i}{x_{i-1} - x_i} + T\frac{y_{i+1} - y_i}{x_{i+1} - x_i} \tag{3.5}$$

Let us make the additional simplifying assumptions that all the springs are uniformly spaced ($\forall i, x_i - x_{i-1} = \Delta x$), are of equal stiffness k, and that the relaxed spring length $y_0 = 0$. We can then rewrite Equation 3.5 as

$$-y_{i-1} + \left(2 + \frac{\Delta x}{T}k\right)y_i - y_{i+1} = \frac{\Delta x}{T}ku_i \tag{3.6}$$

Observe that the left-hand-side of Equation 3.6 is linear in the unknown displacements y_i, and the right-hand-side is linear in the input displacements u_i. We can therefore write the entire system of equations resulting from applying the static balance condition along the entire length of the cable as a matrix equation, as follows.

Define the symbol $\varepsilon = \frac{\Delta x}{T}k$. Then the matrix equation obtained by repeating Equation 3.6 for every spring point along the cable from Spring 1 to n has the form:

$$\underbrace{\begin{bmatrix} 1+\varepsilon & -1 & & & & & \\ -1 & 2+\varepsilon & -1 & & & & \\ & \ddots & \ddots & \ddots & & & \\ & & -1 & 2+\varepsilon & -1 & & \\ & & & & \ddots & & \\ & & & & -1 & 1+\varepsilon \end{bmatrix}}_{\mathbf{M}} \begin{bmatrix} y_1 \\ y_2 \\ \vdots \\ y_i \\ \vdots \\ y_n \end{bmatrix} = \begin{bmatrix} \varepsilon u_i \\ \varepsilon u_2 \\ \vdots \\ \varepsilon u_i \\ \vdots \\ \varepsilon u_n \end{bmatrix} \tag{3.7}$$

The matrix $\frac{1}{\varepsilon}\mathbf{M} = \mathbf{K}$ is the stiffness matrix of the system, and gives the kinematic relationship between the cable displacements y and the inputs u.

3.2 Influence Matrix for the Taught Cable Supported by Springs

Because the kinematics defined Equation 3.7 are linear, the deformed shape of the entire cable in response to any combined actuator input can be decomposed into a sum of response shapes resulting from the individual ON actuators in that input. Thus, in order to fully understand the discrete nature of the actuation in this mechanism, it is necessary to determine an expression for the influence of each actuator on entire cable.

To do this, observe that $\mathbf{K}^{-1}\vec{u} = \varepsilon\mathbf{M}^{-1}\vec{u} = \vec{y}$. That is, the i^{th} column of $\mathbf{K}^{-1}$ is the vector $\vec{y}$ of vertical displacements of the *entire* cable that result from the application of a single unit displacement at the base of the i^{th} spring. This section will derive the columns of the influence matrix $\mathbf{K}^{-1}$ analytically.

Factoring out the constant ε, the task of inverting $\mathbf{K}$ reduces to inverting $\mathbf{M}$. This matrix has a simple structure, and is easy to invert analytically. Following the methods of [26], we construct the inverse by elimination. Consider the first few steps of the forward elimination:

$$\begin{bmatrix} \overbrace{1+\varepsilon}^{p_1} & -1 & & \\ -1 & 2+\varepsilon & -1 & \\ & -1 & 2+\varepsilon & -1 \\ & & \ddots & \ddots \end{bmatrix} \rightarrow \begin{bmatrix} 1+\varepsilon & -1 & & \\ & \overbrace{2+\varepsilon-\frac{1}{1+\varepsilon}}^{p_2} & & \\ 0 & -1 & & \\ & \ddots & \ddots & \ddots \end{bmatrix} \tag{3.8}$$

The first pivot of the matrix $\mathbf{M}$ is the first entry. Notice that because the matrix is tridiagonal, each pivot is only used for the row below it in the forward elimination. Therefore, when we consider the i^{th} row of the forward elimination, we need only

keep track of the pivot p_{i-1} from the previous step.

$$\begin{bmatrix} \ddots & & & & \\ & 0 & p_i & -1 & \\ & & -1 & 2+\varepsilon & -1 \\ & & & & \ddots \end{bmatrix} \rightarrow \begin{bmatrix} \ddots & & & & \\ & 0 & p_i & -1 & \\ & & 0 & \underbrace{2+\varepsilon-\frac{1}{p_i}}_{p_{i+1}} & -1 \\ & & & & \ddots \end{bmatrix} \tag{3.9}$$

From this, it is evident that in the interior of the matrix, the following relation holds between neighboring pivots:

$$p_{i+1} = 2 + \varepsilon - \frac{1}{p_i} \tag{3.10}$$

This relation defines a discrete pivot dynamics that evolves down the rows of the matrix during forward elimination. To find the fixed points of this dynamics, we write the discrete difference of the pivots

$$p_{i+1} - p_i = 2 + \varepsilon - \frac{1}{p_i} - p_i \tag{3.11}$$

Rearranging,

$$p_{i+1} - p_i = \frac{-p_i^2 + (2+\varepsilon)\, p_i - 1}{p_i} \tag{3.12}$$

Figure 3-3 plots the value of the numerator of 3.12. The two zeros of the numerator occur at nonzero values of the pivot in the denominator and therefore represent the two fixed points of 3.11. The fixed points at $p = 1 + \frac{\varepsilon}{2} - \sqrt{\varepsilon + \frac{\varepsilon^2}{4}}$ is clearly unstable, as evidenced by the sign of the curve, and the fixed point at $p = 1 + \frac{\varepsilon}{2} + \sqrt{\varepsilon + \frac{\varepsilon^2}{4}}$ is locally stable.

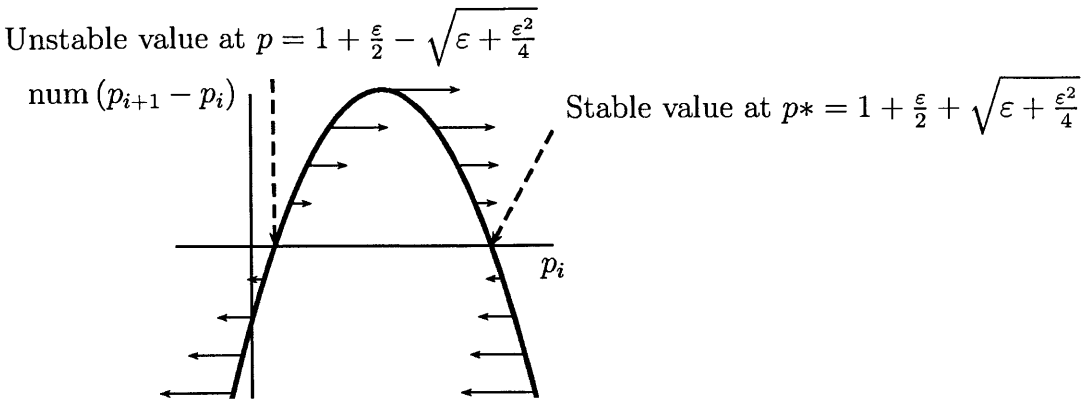

Figure 3-3: Pivot Dynamics During Forward Elimination of Stiffness Matrix. Plot of Numerator of Δp vs p. Arrows indicate direction of increment of next value of p, derived from the sign and magnitude of the curve.

Claim 3.1. *The region of attraction of the stable pivot at* $p* = 1 + \frac{\varepsilon}{2} + \sqrt{\varepsilon + \frac{\varepsilon^2}{4}}$ *begins at the unstable pivot and goes to infinity.*

Proof. We begin by considering the region to the right of $p*$. We would like to show that $p_i > p* \implies p* < p_{i+1} < p_i$.

We begin by proving the first inequality. Assume as a contradiction that $p_{i+1} < p*$. That is,

$$p_{i+1} = 2 + \varepsilon - \frac{1}{p_i} < p*$$

Substituting in the value of $p*$,

$$2 + \varepsilon - \frac{1}{p_i} < 1 + \frac{\varepsilon}{2} + \sqrt{\varepsilon + \frac{\varepsilon^2}{4}}$$

Canceling terms and rearranging,

$$\frac{1}{p_i} > 1 + \frac{\varepsilon}{2} - \sqrt{\varepsilon + \frac{\varepsilon^2}{4}} \tag{3.13}$$

Observe that the term in the square root can be rewritten as $\varepsilon + \frac{\varepsilon^2}{4} = \left(1 + \frac{\varepsilon}{2}\right)^2 - 1$. Therefore,

$$\varepsilon + \frac{\varepsilon^2}{4} < 1 + \varepsilon + \frac{\varepsilon^2}{4} = \left(1 + \frac{\varepsilon}{2}\right)^2$$

and thus,

$$\sqrt{\varepsilon + \frac{\varepsilon^2}{4}} < 1 + \frac{\varepsilon}{2} \iff 0 < 1 + \frac{\varepsilon}{2} - \sqrt{\varepsilon + \frac{\varepsilon^2}{4}} \tag{3.14}$$

Inequality 3.14 implies that the right-hand-side of Inequality 3.13 is strictly positive, allowing us to invert both sides,

$$p_i < \frac{1}{1 + \frac{\varepsilon}{2} - \sqrt{\varepsilon + \frac{\varepsilon^2}{4}}}$$

By our initial definition, $p* < p_i$, and thus

$$1 + \frac{\varepsilon}{2} + \sqrt{\varepsilon + \frac{\varepsilon^2}{4}} = p* < \frac{1}{1 + \frac{\varepsilon}{2} - \sqrt{\varepsilon + \frac{\varepsilon^2}{4}}}$$

Rearranging and combining terms,

$$\begin{aligned}
\left(1 + \frac{\varepsilon}{2} + \sqrt{\varepsilon + \frac{\varepsilon^2}{4}}\right)\left(1 + \frac{\varepsilon}{2} - \sqrt{\varepsilon + \frac{\varepsilon^2}{4}}\right) &< 1 \\
\left(1 + \frac{\varepsilon}{2}\right)^2 - \left(\varepsilon + \frac{\varepsilon^2}{4}\right) &< 1 \\
1 + \varepsilon + \frac{\varepsilon^2}{4} - \varepsilon - \frac{\varepsilon^2}{4} &< 1 \\
1 &< 1 \text{ ↯}
\end{aligned}$$

Before we prove the second inequality, consider the quantity $p_i - \left(1 + \frac{\varepsilon}{2}\right)$. By our original definition, $p_i > p^* = 1 + \frac{\varepsilon}{2} + \sqrt{\varepsilon + \frac{\varepsilon^2}{4}} \implies p_i - \left(1 + \frac{\varepsilon}{2}\right) > \sqrt{\varepsilon + \frac{\varepsilon^2}{4}}$.

Squaring, we have that

$$\varepsilon + \frac{\varepsilon^2}{4} < \left(p_i - \left(1 + \frac{\varepsilon}{2}\right)\right)^2 \tag{3.15}$$

Now, assume by contradiction that $p_{i+1} > p_i$. That is,

$$\begin{aligned}
2 + \varepsilon - \frac{1}{p_i} &> p_i \\
0 &> p_i^2 - p_i(2+\varepsilon) + 1 \\
0 &> \left(p_i - \left(1 + \frac{\varepsilon}{2}\right)\right)^2 + 1 - \left(1 + \frac{\varepsilon}{2}\right)^2 \\
0 &> \left(p_i - \left(1 + \frac{\varepsilon}{2}\right)\right)^2 - \left(\varepsilon + \frac{\varepsilon^2}{4}\right) \\
\left(\varepsilon + \frac{\varepsilon^2}{4}\right) &> \left(p_i - \left(1 + \frac{\varepsilon}{2}\right)\right)^2 \text{ ↯ by 3.15}
\end{aligned}$$

Thus far, we have shown that the entire region to the right of the stable fixed point is within the region of attraction. What is more, we have shown that any initial condition in that region will remain in that region and decay monotonically to $p*$. To show that the interval between the unstable and stable fixed points is within the region of attraction of $p*$, we need only show that $p_i < p* \implies p_{i+1} > p_i$. We need not concern ourselves with showing that $p_{i+1} < p*$ because we have just shown that if the pivot "escapes" into the region $p_{i+1} > p*$, it will remain in that region and decay down to $p*$, precluding the possibility of oscillation.

This proof that $p_i < p* \implies p_{i+1} > p_i$ is trivial: by Figure 3-3, the sign of $p_{i+1} - p_i$ in the region between the fixed points is strictly positive, and thus, any initial pivot in that region will increase.

This completes the proof that the region of attraction for the fixed point at $p* = 1 + \frac{\varepsilon}{2} + \sqrt{\varepsilon + \frac{\varepsilon^2}{4}}$ spans from the unstable fixed point at $1 + \frac{\varepsilon}{2} - \sqrt{\varepsilon + \frac{\varepsilon^2}{4}}$ to infinity. □

To show that the pivots converge during forward elimination, we must show that the initial pivot p_1 from the first step of the forward elimination falls within the basin of attraction of the stable fixed point $p*$. From Equation 3.8, we know that $p_1 = 1 + \varepsilon$, and we must verify that

$$1 + \varepsilon \overset{?}{>} 1 + \frac{\varepsilon}{2} - \sqrt{\varepsilon + \frac{\varepsilon^2}{4}} \iff \frac{\varepsilon}{2} \overset{?}{>} -\sqrt{\varepsilon + \frac{\varepsilon^2}{4}} \tag{3.16}$$

Because $\varepsilon = \Delta x/T$ is a strictly positive quantity, this is trivially true. This shows that the pivots of the matrix stability to $p*$ during the forward elimination step.

Having established that the pivots of the matrix stabilize to $p*$ during forward elimination, we examine the entries of the candidate inverse matrix that have been populated by the forward elimination process. The initial candidate inverse begins as the identity, and after the pivots stabilize, each subsequent row of the candidate inverse is constructed by adding $\frac{1}{p*}$ times the previous row to it, resulting in the transformation

$$\underbrace{\begin{bmatrix} \ddots & & & & & \\ & 1 & & & & \\ & 0 & 1 & & & \\ & 0 & 0 & 1 & & \\ & 0 & 0 & 0 & 1 & \\ & & & & & \ddots \end{bmatrix}}_{\text{Candidate inverse before forward elimination}} \rightarrow \underbrace{\begin{bmatrix} \ddots & & & & & \\ & 1 & & & & \\ & \frac{1}{p*} & 1 & & & \\ & \frac{1}{p*^2} & \frac{1}{p*} & 1 & & \\ & \frac{1}{p*^3} & \frac{1}{p*^2} & \frac{1}{p*} & 1 & \\ & & & & & \ddots \end{bmatrix}}_{\text{Candidate inverse after forward elimination}} \tag{3.17}$$

We now consider the backward elimination process. After the forward elimination

pass, the original matrix **M** has been transformed into

$$\begin{bmatrix} \ddots & & & \\ & p* & -1 & \\ & 0 & p* & -1 \\ & & 0 & \ddots \end{bmatrix}$$

The backward elimination process, therefore, consists of adding to each row exactly $\frac{1}{p*}$ times the row below it, and dividing out the common $p*$ at the end. This operation is performed on the candidate inverse matrix in the right-hand-side of Equation 3.17 as well.

Consider the j^{th} column of the candidate inverse just before the start of backward elimination. By inspection of the right-hand-side of 3.17, the ij^{th} element is given by $\frac{1}{p*^{i-j}}$. Specifically, the bottom of the column contains the terms

$$\begin{bmatrix} \vdots \\ \frac{1}{p*^{n-j-2}} \\ \\ \frac{1}{p*^{n-j-1}} \\ \\ \frac{1}{p*^{n-j}} \end{bmatrix} \tag{3.18}$$

After the first step of backward elimination, the second to last row in 3.18 gets

increased by $\frac{1}{p*}$ times the row below it, yielding

$$\begin{bmatrix} \vdots & & \\ \frac{1}{p*^{n-j-2}} & & \\ \frac{1}{p*^{n-j-1}} & + & \frac{1}{p*}\frac{1}{p*^{n-j}} \\ \frac{1}{p*}\nearrow & & \\ \frac{1}{p*^{n-j}} & & \end{bmatrix} \tag{3.19}$$

After the second step of backward elimination, *each term* in the second-to-last row is multiplied by $\frac{1}{p*}$ and added to the row above it:

$$\begin{bmatrix} \vdots & & & \\ \frac{1}{p*^{n-j-2}} & + & \frac{1}{p*}\frac{1}{p*^{n-j-1}} & + & \frac{1}{p*^2}\frac{1}{p*^{n-j}} \\ \frac{1}{p*}\nearrow & & \frac{1}{p*}\nearrow & & \\ \frac{1}{p*^{n-j-1}} & + & \frac{1}{p*}\frac{1}{p*^{n-j}} & & \\ \frac{1}{p*}\nearrow & & & & \\ \frac{1}{p*^{n-j}} & & & & \end{bmatrix} \tag{3.20}$$

By inspection of this process, it is apparent that the number of terms added to a given row after backward elimination is equal to the height of that row above the bottom of the matrix. Before backward elimination, the term in the ij^{th} entry is given by $\frac{1}{p*^{i-j}}$. If the matrix is $n \times n$, during backward elimination, exactly $n - i$ terms get added to this entry. By inspection of Equation 3.20, it is evident that the ij^{th} entry of the candidate inverse after the backward elimination is completed and

the extra factor of $p*$ is divided out from the main diagonal will be

$$\left(\mathbf{M}^{-1}\right)_{ij} = \frac{1}{p*} \sum_{v=0}^{v=n-i} \frac{1}{p*^{v}} \frac{1}{p*^{i-j+v}} \tag{3.21}$$

Factoring out the constant terms and applying the well-known geometric sum identity $\sum_{k=0}^{L} a^k = \frac{1-a^{L+1}}{1-a}$, we have that

$$\left(\mathbf{M}^{-1}\right)_{ij} = \frac{1}{p*^{i-j}} \frac{1 - \left(p*^{-2(n-i+1)}\right)}{p* - \frac{1}{p*}} \tag{3.22}$$

In the central column of the matrix, $n - i + 1$ is a large number. Because $\varepsilon > 0$, by Inequality 3.14 $p* = 1 + \frac{\varepsilon}{2} - \sqrt{\varepsilon + \frac{\varepsilon^2}{4}} > 1$. Therefore, the numerator $1 - \left(p*^{-2(n-i+1)}\right) \approx 1$. Thus, in the center of the matrix, where the pivot has stabilized to $p*$, the elements of the influence matrix $\mathbf{K}^{-1}$ can be approximated as

$$\left(\mathbf{K}^{-1}\right)_{ij} \approx \frac{\varepsilon}{p* - \frac{1}{p*}} \frac{1}{p*^{i-j}} \tag{3.23}$$

Recalling the inverse kinematic relation $\vec{y} = \mathbf{K}^{-1}\vec{u}$, we can say that that the vertical displacement y of the cable above the central spring in response to a displacement u_w imposed on the base of a spring located $w\Delta x$ units away from the center is given by

$$y = u_w \frac{\varepsilon}{p* - \frac{1}{p*}} p*^{-w} \tag{3.24}$$

In words, Equation 3.24 states that the influence of a constant magnitude actuation on the center of the cable *decays exponentially* with horizontal distance of the actuation point from the center of the cable. Because $p*$ is an increasing function of the stiffness ratio ε, the mechanical properties of the mechanism (spring rates,

spring spacing, cable tension) can be adjusted such that the decay factor $p*$ is some integer root of 2, realizing the requirement that the decay factor between different actuators is exactly 1/2 for constant magnitude actuation.

3.3 Stiff Beam on an Elastic Foundation

The search for elastic mechanisms with purely exponential decay of actuator influence is motivated by the desire to use identical actuators in the entire mechanism. While this desire is reasonable, a somewhat looser requirement on the actuators employed in a practical design is not that they necessarily be identical, but that they not require a large dynamic range of accuracy in their manufacturing process. This looser requirement opens a wider class of compliant mechanisms for use in binary mechatronic design. This section will present one such class of mechanism, based on the deformation of a stiff beam resting on an elastic foundation.

A stiff beam resting on a continuous elastic foundation will deform in response to a force directed into its top surface. Assuming that the beam is narrow and the inputs are small, it is appropriate to analyze the problem in the planar case. Consider the case of a unit magnitude point load applied to the beam, as shown in Figure 3-4. From well-developed elasticity theory [29] [18], it is known that the deflection of the beam surface is governed by

$$\frac{d^2}{dx^2}\left(EI\frac{d^2y}{dx^2}\right) + ky = \delta(x) \tag{3.25}$$

where EI is the flexural rigidity of the beam, k is the spring rate density of the elastic support, and $\delta(x)$ represents a unit force point load.

Defining the length constant $\kappa = \left(\frac{k}{4EI}\right)^{1/4}$, the solution for the vertical deflection

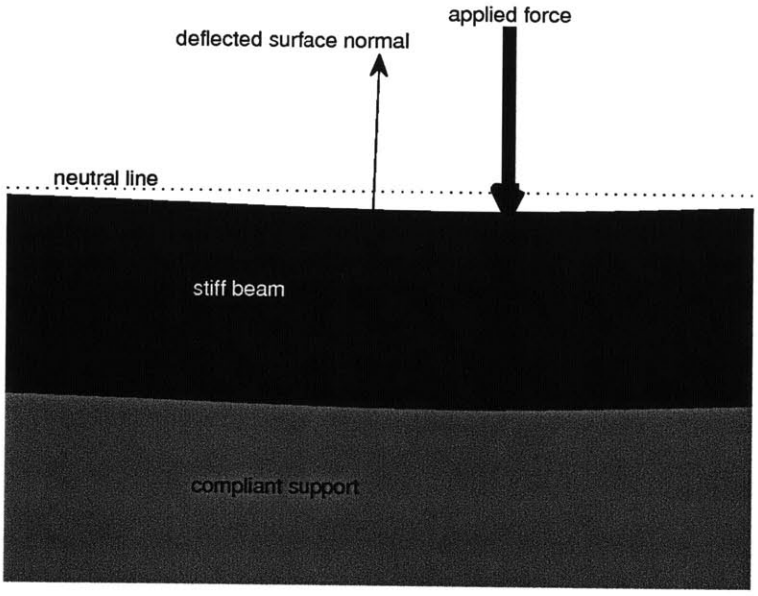

Figure 3-4: Deformation of Stiff Beam on Elastic Foundation

of the beam at a distance x away from the application point is given by

$$y = \frac{1}{8\kappa^3} e^{-|\kappa x|} \left(\cos \kappa x + \sin |\kappa x|\right) \tag{3.26}$$

and the solution for the angular deflection is

$$\theta = -\frac{1}{4\kappa^2} e^{-|\kappa x|} \sin \kappa x \tag{3.27}$$

Observe that the expressions for both the displacement and angular deflection contain an exponential decay term. Drawing inspiration from the concept of computed torque control in dynamics [25], we place the i^{th} actuator at $x_i = i \log 2/\kappa$ distance units away from our chosen measurement point, making the exponential $e^{-|\kappa| i \log 2/\kappa} = 2^{-i}$, and select the ON force magnitude of the i^{th} actuator to be $b_i = 1/\left(\cos \kappa x_i + \sin |\kappa x_i|\right)$, canceling out the oscillatory terms and yielding a purely exponential decay of actuator influence magnitudes on the measurement point at $x = 0$. Alternatively, we can select the actuator magnitudes as $b_i = 1/\sin \kappa x_i$ in order to control the angular deflection of the center of the beam.

While the actuator magnitudes required to achieve a uniform output coordinate density in vertical displacement or in deflection angle are no longer identical, the elastic averaging in the mechanism enables, with judicious selection of mechanism parameters and force point spacing, the realization of high resolution output with a looser requirement on the dynamic range of the force actuators themselves than would be achievable without exploiting elasticity.

Chapter 4

Extension to Optimal Kinematics For Multiple Independent Degrees of Freedom

The original motivation of this line of research was to determine if there exists a truss and binary actuator geometry which can optimally control a two-dimensional deformable surface that is part of a three-dimensional optical system. The results of the previous chapter suggest that there exist compliant mechanisms that allow constant or near-constant magnitude actuators to apply exponentially decaying influences on the position of a single point on the mechanism, allowing the optimal uniform density to be achieved at that point. The question then naturally arises: is this extensible to a design for simultaneous independent control of multiple adjacent points on a surface as required for active optics?

Before considering this question, an important subtlety must be emphasized: the design for binary mechatronic control of multiple independent points on a surface

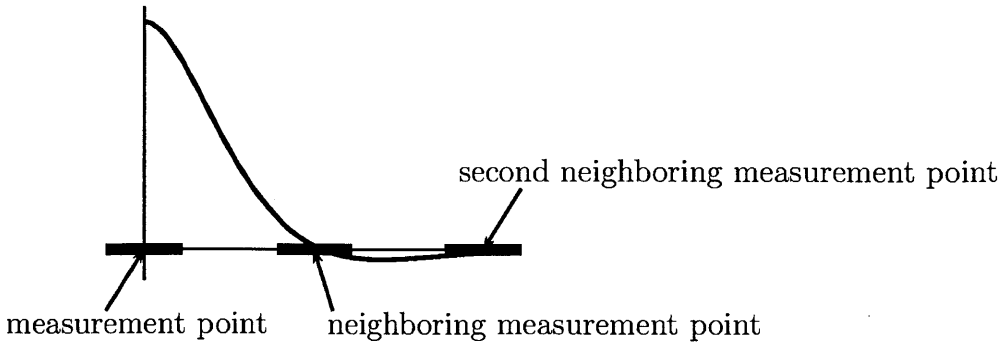

Figure 4-1: Ideal Actuator Influence Function in Typical Adaptive Optics Deformable Mirror [30]

must be done in a way that is amenable to optical wavefront correction. Because the figure of an optical surface must be controlled to a given precision over the *entirety* of the surface and not just at a discrete set of measurement points distributed over the surface, the influence of *all* binary actuators must be restricted to a local neighborhood of the point which they actuate.

Consider Figure 4-1, paraphrased from [30], which shows the influence function of a single (continuous) actuator in a typical deformable mirror with many neighboring (continuous) actuators. Because this design assumes a continuous linear actuator positioned below the surface of the mirror, the influence function in Figure 4-1 has the same (localized) shape for all actuation magnitudes of that actuator.

In designing a binary actuator configuration to replace the continuous actuator, we must avoid the kind of situation shown in Figure 4-2, where the influence of each binary actuator is indeed localized to the region of the actuator, but the resulting shape over the *entire surface* in the neighborhood of the measurement point contains spurious displacements, which are not conducive to accurate wavefront correction.

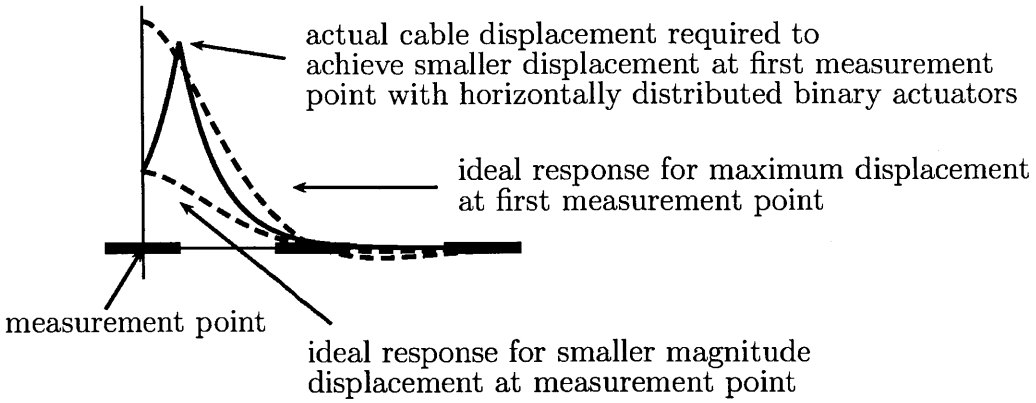

Figure 4-2: Spurious Displacement Between Measurement Points Under Naive Binary Actuation

This Chapter will address these issues by presenting a mechanism geometry that preserves the exponential decay of actuator influences on a set of surface points, but maintains locality of a set of actuators to the region of their respective surface point by directing the spurious displacements into the third dimension, away from the optical surface and into the interior of the surface support structure where they have no effect on any optical element exposed to the incoming wavefront. Figure 4-3 shows a planar truss composed of active elastic members. This mechanism can be thought of as a two-dimensional slice of a three-dimensional optical system, and will serve as the basis for the design philosophy presented in this chapter.

The remainder of this Chapter is organized as follows: First, Section 4.1 will present a graphical proof that will demonstrate that the influence of binary displacement actuators in the interior of this planar truss on its top surface can be approximated by the same influence function that models taught cable system, where the exponential decay occurs in the vertical direction (into the interior of the truss) rather than the horizontal direction along the top surface.

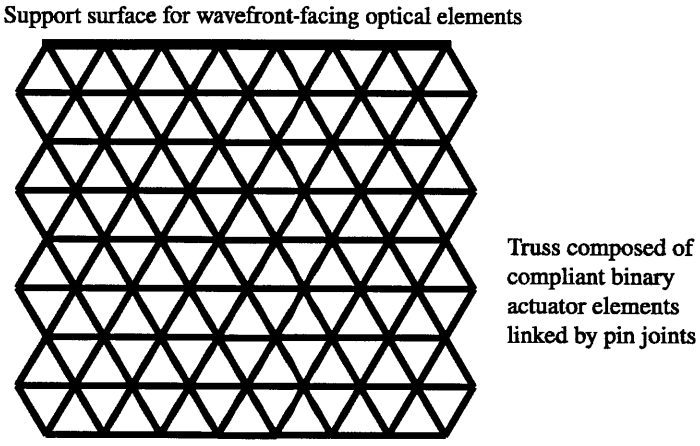

Figure 4-3: Planar Triangular Binary Truss Structure. The top surface of the truss can either directly support a meniscus-type thin monolithic mirror or individual rigid mirrors in a segmented primary arrangement.

Second, Section 4.2 will validate that approximation with linear and nonlinear simulations of the deformation of the top surface of the truss in response to binary actuation in its interior as a function of the depth of the actuation below the top surface. Specific attention will be paid to the effect of truss geometry, relative stiffness of the truss members, and various boundary conditions on the exponential decay rate of influence.

Finally, Section 4.3 will aggregate the insight gained from this analysis and will present a design for a multi-d.o.f. binary-actuated deformable optical surface capable of achieving independent uniform discrete distributions of vertical displacements for adjacent points on its top surface.

4.1 Approximate Stiffness Matrix for the Planar Truss

This section will derive an approximate analytical form for the influence of binary displacement actuators embedded in the members of the triangular truss mechanism shown in Figure 4-3. Lee showed [14] that if only the top several layers of the structure are considered, then exhaustive enumeration of all possible states of all the truss members demonstrates that superposition does *not* hold for large-stroke actuators near the top of the structure. Therefore, this analysis will be confined to determining the effect of small-stroke actuations deep in the interior of the structure.

First, a word about the overall strategy of this section. Constructing a stiffness matrix for a planar truss is a straight-forward mechanical process. So is numerically inverting it. If, however, the stiffness matrix can be inverted *analytically*, as in Section 3.2, it is possible to prove rigorously the existence of optimal binary actuation. Unfortunately, unlike the simple tridiagonal stiffness matrix of the taught cable mechanism which was extremely simple to invert, the stiffness matrix for this truss is complicated and does not yield a compact and easily-understandable inverse.

Furthermore, attempting to use the tools of continuum mechanics in two dimensions in order to get a favorable analytical result is not promising. Indeed, the Green's Functions in two dimensions for any equation that can be argued to model the in-plane deformation of this mechanism (Poisson, Helmholtz, biharmonic, etc) are not simple analytical functions, but rather series expansions in Bessel functions, Hankel functions, or complex exponentials, depending on the choice of coordinates and parameterizations of boundary conditions [9], [18].

While a power series may accurately model the deformation, and may even agree

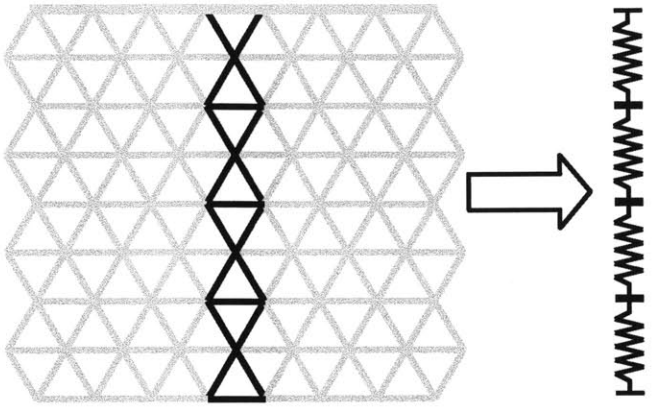

Figure 4-4: Abstraction of a Slice of the Truss

with the numerically inverted stiffness matrix and real experiment, it does not present a particularly fertile starting point for a symbolic proof of the existence of optimal binary actuation in the mechanism. For this reason, exact accuracy will initially be traded for simplicity in the development of an approximate form for the influence of the truss members in the interior of the structure on the top surface, and the overall theme of this section will be to argue that the easily-invertible stiffness matrix of the taught cable mechanism is applicable to this truss.

Consider a single column of "V" elements of the truss, and neglect (for the time being) the coupling between that column and its immediate neighbors. Then as shown in Figure 4-4, the column can be approximated as a column of linear springs. The stiffness matrix for a column of springs is almost identical to the stiffness matrix for the taught cable system. Indeed, while the stiffness matrix for the taught cable system has rows of the form $[-1, 2+\varepsilon, -1]$, the stiffness matrix for a column of springs connected in series as shown in Figure 4-4 consists of rows of the form

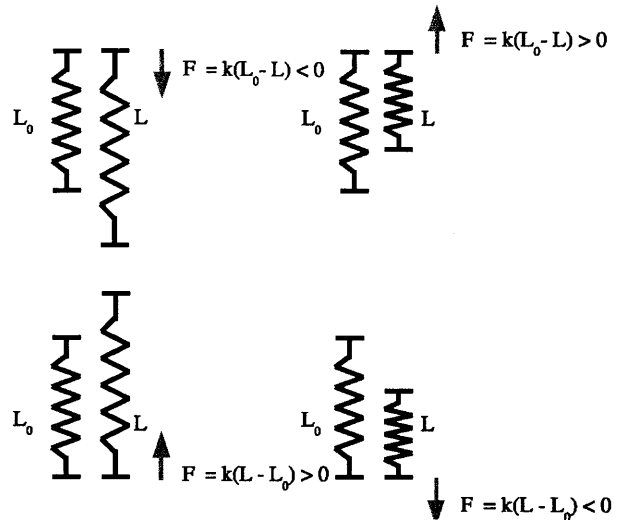

Figure 4-5: Sign Conventions for Forces in Column of Springs

$[-1, 2, -1]$, [26].

Before going into further detail, it is worth defining sign conventions used for the lengths, displacements, and forces used in the analysis of this mechanism. Figure 4-5 illustrates the sign conventions for the forces at the nodes of the mechanism. Assuming all spring lengths (relaxed, stretched, or compressed) are strictly positive quantities, then the magnitude of the spring force is given by the difference between the relaxed and compressed/stretched length, but the sign depends on whether the measurement is taken at the "top" or "bottom" of the spring with respect to the canonical "up" direction.

Figure 4-6, shows the static force balance conditions in the interior of the column in response to an imposed vertical force load u_i, using the sign conventions from Figure 4-5. Symbolically,

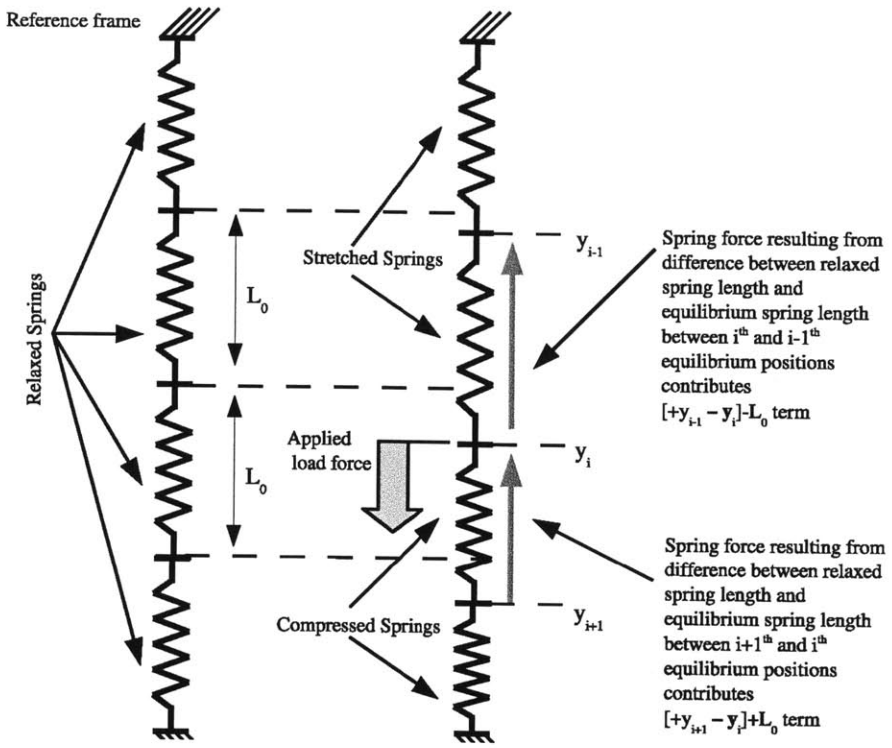

Figure 4-6: Force Balance in Column of Springs with Force Input

$$0 = u_i + k\left(\underbrace{y_{i-1} - y_i}_{L \text{ from Figure 4-5}} - L_0\right) + k\left(\underbrace{y_{i+1} - y_i}_{-L \text{ from Figure 4-5}} + L_0\right) \tag{4.1}$$

When terms cancel and are appropriately combined, we re-write Equation 4.1 as the row of a (larger) stiffness matrix, with the row equation given by

$$[-1, 2, -1]\begin{bmatrix} y_{i-1} \\ y_i \\ y_{i+1} \end{bmatrix} = \frac{1}{k}u_i \tag{4.2}$$

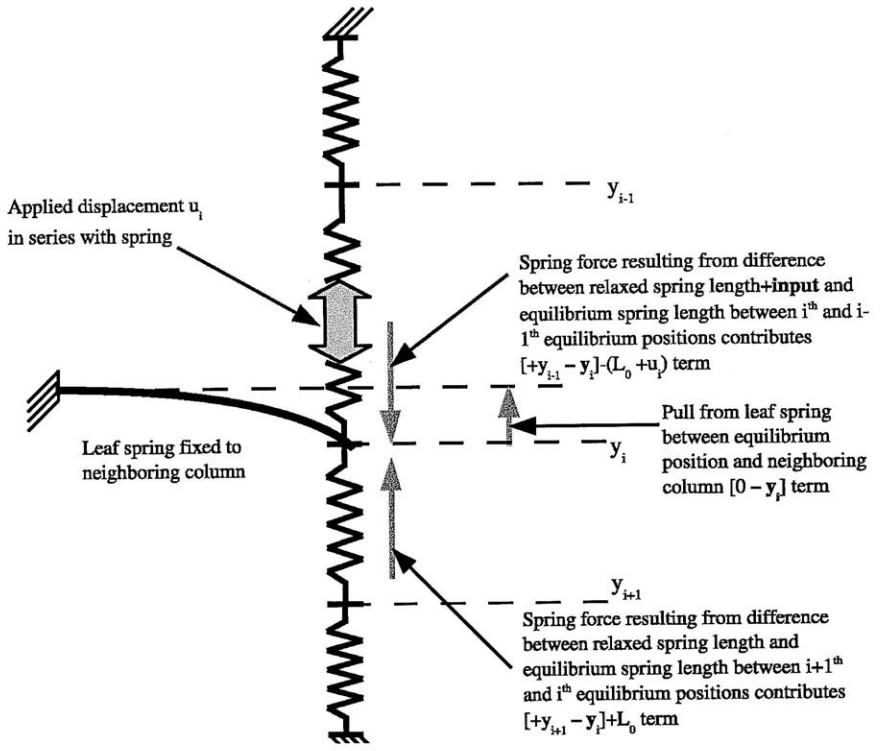

Figure 4-7: Force Balance in Column of Springs Coupled to Ground with Series Displacement Input

Now consider Figure 4-7, which replaces the parallel force actuation with is equivalent series displacement and adds a leaf spring from the interior nodes to an infinitely stiff reference frame in the neighboring column. While the infinite stiffness of the neighboring column is not physical, it serves as a potentially plausible, and convenient, approximation for the purposes of deriving an analytical form for the response of the truss.

If the leaf spring vertical stiffness is given by k_l and the column member stiffness

by k_s, the force balance equation is

$$0 = \underbrace{k_l\,(0 - y_i)}_{\text{pull to neighboring column}} + \underbrace{k_s\,(y_{i-1} - y_i - L_0 - u_i)}_{\text{upper spring with input}} + \underbrace{k_s\,(y_{i+1} - y_i + L_0 + u_{i+1})}_{\text{lower spring}} \tag{4.3}$$

which in stiffness matrix form looks like

$$\left[-1, 2 + \frac{k_l}{k_s}, -1\right] \begin{bmatrix} y_{i-1} \\ y_i \\ y_{i+1} \end{bmatrix} = [1, -1] \begin{bmatrix} u_i \\ u_{i+1} \end{bmatrix} \tag{4.4}$$

Overall,

$$\underbrace{\begin{bmatrix} 1+\frac{k_l}{k_s} & -1 & & & \\ \ddots & \ddots & \ddots & & \\ & -1 & 2+\frac{k_l}{k_s} & -1 & \\ & & & \ddots & \\ & & & -1 & 1+\frac{k_l}{k_s} \end{bmatrix}}_{\mathbf{M}} \begin{bmatrix} y_1 \\ \vdots \\ y_i \\ \vdots \\ y_n \end{bmatrix} = \underbrace{\begin{bmatrix} 1 & -1 & & & \\ & \ddots & \ddots & & \\ & & 1 & -1 & \\ & & & \ddots & \\ & & & & 1 \end{bmatrix}}_{\mathbf{T}} \begin{bmatrix} u_1 \\ \vdots \\ u_i \\ \vdots \\ u_n \end{bmatrix} \tag{4.5}$$

The influence of actuators on vertical displacements of the nodes is therefore given by

$$\vec{y} = \mathbf{M}^{-1}\mathbf{T}\vec{u} \tag{4.6}$$

where by the positivity of the stiffness ratio k_l/k_s, $\mathbf{M}^{-1}$ has the same form as derived for the taught cable system, namely exponential decays. While at first glance, the differentiation matrix $\mathbf{T}$ would would appear to make this an entirely different influence matrix from that derived for taught cable, the key observation is that because the measurement point is on the top surface of the structure, only the first row of

the influence matrix affects it.

Because $\mathbf{T}$ is a discrete difference matrix, the top row of the product $\mathbf{M}^{-1}\mathbf{T}$ is given by the discrete difference of the top row of $\mathbf{M}^{-1}$. But because the top row of $\mathbf{M}^{-1}$ is a decaying exponential, *the discrete difference of the top row is also a decaying exponential*, and thus the top row of the influence matrix is a decaying exponential, implying that the influence on the vertical displacement of the top of the column of actuators in the interior of the column decays exponentially with depth, as required for optimality, and because the "spurious displacements" associated with individual bits occur in the interior of the structure, if the approximation developed thus far holds, this arrangement is a suitable basis for a practical design for binary mechatronic optical figure correction.

4.2 Numerical Validation Experiments in Two Dimensions

The initial validation of the admittedly intuitive argument presented in the previous section was accomplished by examining the truss structure such as the one shown in Figure 4-3. Specifically, the first question meant to be answered by initial numerical experimentation was whether or not the elastic truss in Figure 4-3, when subjected to constant magnitude binary actuation of some subset of its members, exhibited exponential decay of influence on the vertical displacement of the top surface of the truss, where the decay was exponential with increasing depth of the actuator from the top surface.

Approaching the problem with limited insight about the relative magnitudes of the effects of different boundary conditions, truss geometry, and rotation-induced

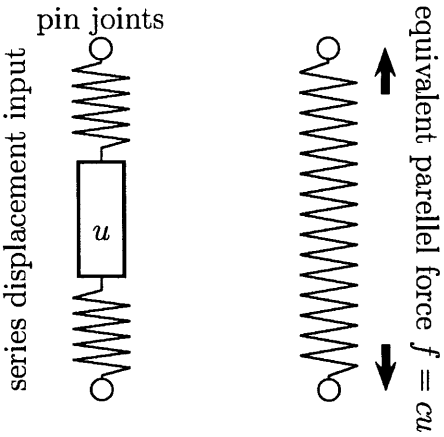

Figure 4-8: Detail of Model of Truss Member

nonlinearity, but mindful of Lee and Bilton's result that nonlinearity plays a significant role whenever actuation magnitude exceeds a non-negligible fraction of the truss member length, it was felt that a purely linear analysis of the truss (that is, just simply inversion of its stiffness matrix) was possibly insufficient to capture the behavior of the mechanism. Therefore, the iterative routine detailed in Algorithm 1, was used to solve for the truss deformation.

The actuation model implemented in the code is shown in Figure 4-8. For convenience of coding, the latter definition of equivalent parallel force was used in the implementation.

Algorithm 1 Algorithm for Computing Nonlinear Effects in Deformation of Truss

$\mathbf{x} \leftarrow$ node geometry
$\mathbb{E} \leftarrow$ link geometry
$\mathbf{C} \leftarrow$ link spring rates
$\mathbf{a} \leftarrow$ actuator displacements
$tol \leftarrow 1 \times 10^{-6}$
$i_{\max} \leftarrow 100$
$\Delta\mathbf{u} \leftarrow \mathbf{0}$
$\Delta\mathbf{x} \leftarrow \mathbf{0}$
$i \leftarrow 1$
while true **do**
  $\mathbf{x}_{\text{new}} \leftarrow \mathbf{x} + \Delta\mathbf{x}$
  $\mathbf{w} \leftarrow$ Internal_Forces $(\mathbf{x}, \mathbf{x}_{\text{new}}, \mathbb{E}, \mathbf{C})$ {Internal force $= c\Delta L$}
  $\mathbf{w}_{\text{residual}} \leftarrow \mathbf{w} + \mathbf{Ca}$ {Actuation transformed into a force}
  $[\mathbf{K}_{\text{new}}, \mathbf{A}_{\text{new}}] \leftarrow$ Stiffness_Matrix $(\mathbf{x}_{\text{new}}, \mathbb{E}, \mathbf{C})$
  $\Delta\mathbf{u} \leftarrow 0.5\mathbf{K}_{\text{new}}^{-1}\mathbf{A}_{\text{new}}^{t}\mathbf{w}_{\text{residual}}$
  if $\Delta\mathbf{u} < tol$ **then**
    break
  end if
  $\Delta\mathbf{x} \leftarrow \Delta\mathbf{x} + \Delta\mathbf{u}$
  $i \leftarrow i + 1$
  if $i > i_{\max}$ **then**
    error
  end if
end while

4.2.1 Validation of Exponential Decay of Influence With Depth

The initial parameters of the structure were chosen so that the mechanism was approximately square, composed of 30 rows, each of 31 equilateral triangles, with each member of unit length unit length and unit stiffness. For these initial experiments, the boundary condition was applied to the bottom nodes of the truss only.

The purpose of this initial exploration was to validate exponential decay of actuator influence with increasing depth from the surface. Unit magnitude actuation was applied symmetrically to the 30 center "V" elements shown in bold in Figure 4-9, and the resulting vertical displacement of the top center of the truss was taken as the output.

Figure 4-10 shows the result of this initial experiment. While there are significant boundary effects near the top of the truss, where the shallower actuator depth gives a more direct line to influence the top, there does indeed exist a small region of approximately constant exponential decay in the bottom half of the truss. Although this region is small, and indeed the magnitude spanned between the actuators in the 10^{th} and 29^{th} rows is only one factor of 2 (only a single bit's worth of difference), this result was considered encouraging.

4.2.2 Sensitivity of Decay Rate to Relative Stiffness of Truss Members

Given the small slope of the region of exponential decay in Figure 4-10, a series of investigations were performed to determine if modifications to the truss stiffness parameters, boundary conditions, or geometry could increase the size of the region over which exponential decay exists and to modify the rate of decay within that region so that a more practical dynamic range of influence could be achieved within

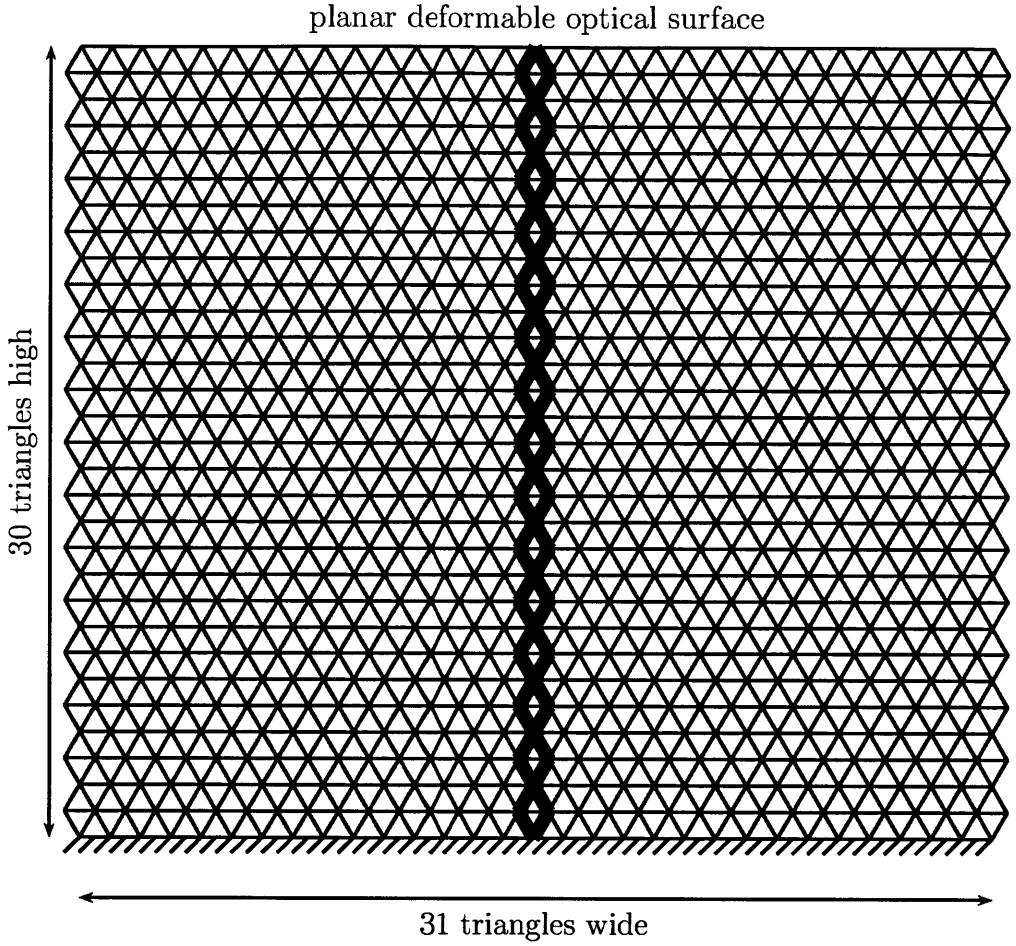

Figure 4-9: Two-Dimensional Truss Used in Initial Validation Simulation. All truss members are unit length and unit stiffness. Unit magnitude actuation force was applied in parallel with bold-faced truss members in the center.

it.

Looking back to the analytical form of the approximation of the influence matrix

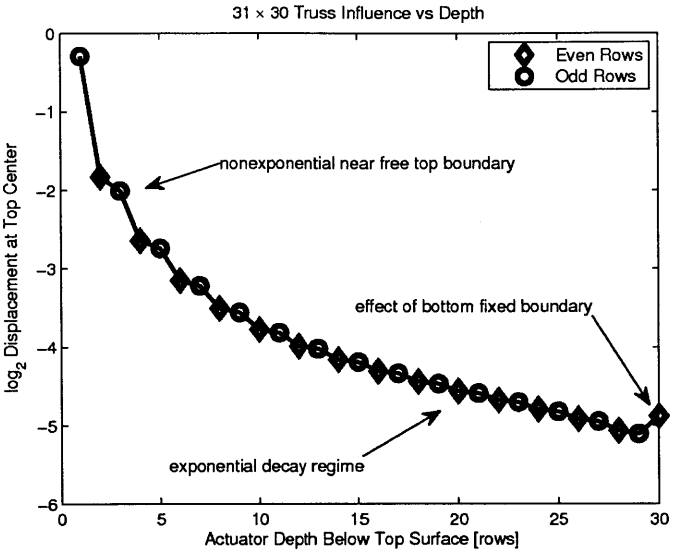

Figure 4-10: Result of Initial Numerical Experiment with 30×31 Truss

from Section 3.2, the magnitude influence as a function of depth w is given by

$$y(w) \propto \frac{1}{p*^w} \tag{4.7}$$

where the ratio $p*$ of successive influence magnitudes is given by

$$p* = 1 + \frac{\varepsilon}{2} + \sqrt{\varepsilon + \frac{\varepsilon^2}{4}} \tag{4.8}$$

where ε is the ratio of the spring rate between adjacent nodes and the spring rate between the nodes and ground. In the analysis of the truss, the approximation was made that the "ground" in question is actually the adjacent column in the truss. Continuing this approximation, an attempt to vary the parameter ε was made by changing the stiffness of the diagonal truss members directly adjacent to the central

column.

Figure 4-11 shows the result of linear and nonlinear simulations of a 31-column wide truss with unit stiffness for the central actuated column and various stiffnesses of the neighboring columns. Because the region of exponential decay in the 30-row high truss was so small, these simulations were run on 60- and 120-row high truss to remove the influence of the bottom boundary on a larger portion of the region of exponential decay. As seen in the result, the effect of varying the stiffness of the neighboring column does not quite have the predicted effect. Using Equation 4.8, varying the stiffness ratio from 0.005 to 0.05 should yield (constant) decay rates ranging from 0.102 bits/row to 0.322 bits/row. While a similar range is seen near the top of the truss, the range in decay rates disappears quickly with depth. In both the 60-row and 120-row trusses, the data suggests a "steady-state" decay rate in the interior of the truss closer to 0.15-0.2 bits/row for all stiffness ratios.

Note also, that in the initial 30-row simulation, all stiffnesses were identical, implying $\varepsilon = 1 \implies \log_2 p* = 1.3$. The magnitude of the decay of influence between the first and second rows in Figure 4-10 is indeed approximately 1.3 bits, validating the approximation near the top of the truss, but demonstrating its limitation as the decay rate drops to less than 0.1 bit/row in the constant decay magnitude region.

At this point, three facts become apparent. The first is that the approximation of the planar truss as a single column of springs breaks down when an attempt is made to modify the decay factor of actuator influences by varying the relative stiffness between adjacent columns, as the approximation would suggest. The second fact is that despite this breakdown in the model, the nonlinear simulation of the $\varepsilon = 0.005$, 120-row case shows that a stable region of approximately 0.15 bits/row influence decay exists. 0.15 bits/row is very close to exactly 7 rows/bit, and while varying the the decay ratio over a large range by pure stiffness modulation seems to fail, the

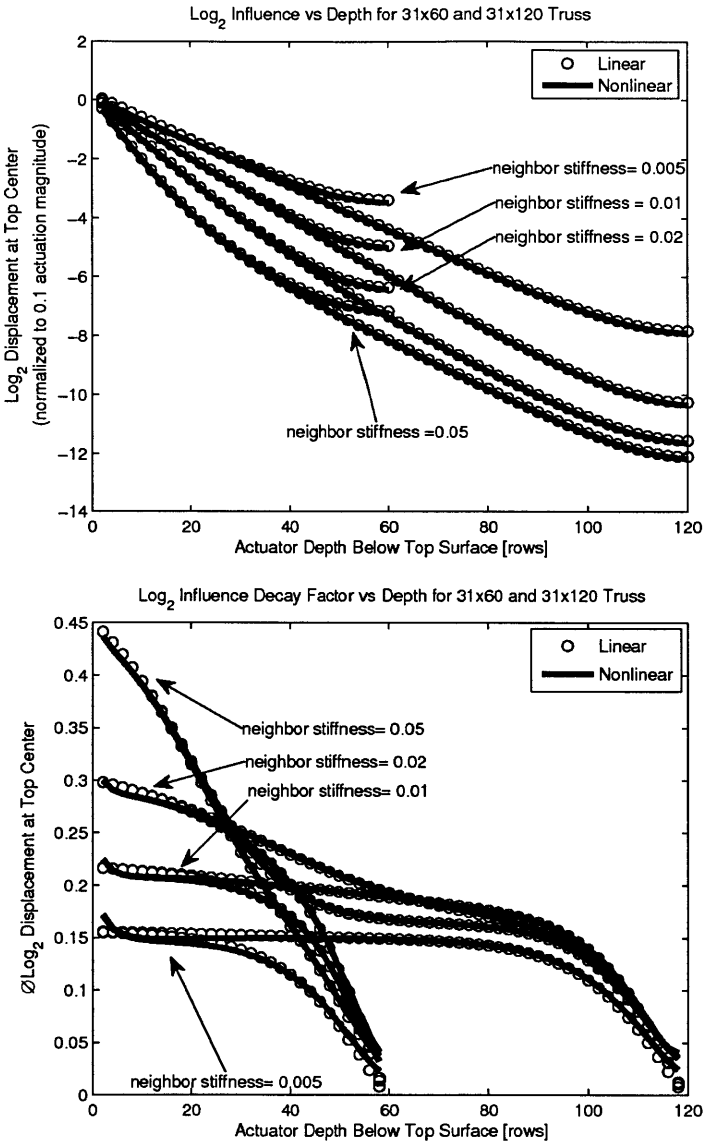

Figure 4-11: Linear and Nonlinear Simulation of Actuator Influence on Top Center Surface of Truss.

data suggests that a small nudge from 0.15 bits/row to exactly 7 rows/bit should be possible over a wide range of depths. Furthermore, in that 120-row case, the region of constant magnitude decay spans over 70 rows, implying that it should be possible to embed a 10-bit actuator in the truss, which is encouraging. Finally, the third fact is that the close agreement between the linear and nonlinear simulation result shown in Figure 4-11 implies that further high-level analysis can be performed to first order without sacrificing much insight, allowing faster computation for further analysis.

4.2.3 Sensitivity of Decay Rate to Truss Geometry

The results of the previous section imply that control of the actuator decay rate by varying the relative stiffnesses of adjacent columns in the truss is not entirely effective, and in order to achieve a large dynamic range with optimal workspace density and inverse kinematics, a very large passive truss structure is required to build up enough dynamic range among the active members of the truss. This may not always be practical if many bits of precision are required but a large truss structure with a decay rate of 7 rows/bit cannot be accommodated.

The approximation employed to derive the decay rate for the truss was based on the assumption that the adjacent column was stiff enough to be modeled as ground. Given the seeming breakdown of this assumption, as series of fast linear simulations were performed to determine the effect of successively wider distances between the active column and the stiff reference. A 240-row truss was simulated with both bottom and side fixed boundary conditions. Figure 4-12 plots the influence vs depth for various widths of the truss.

The result demonstrates that the distance between a stiff reference and the active column has a non-negligible effect on the decay rate of actuator influences on the

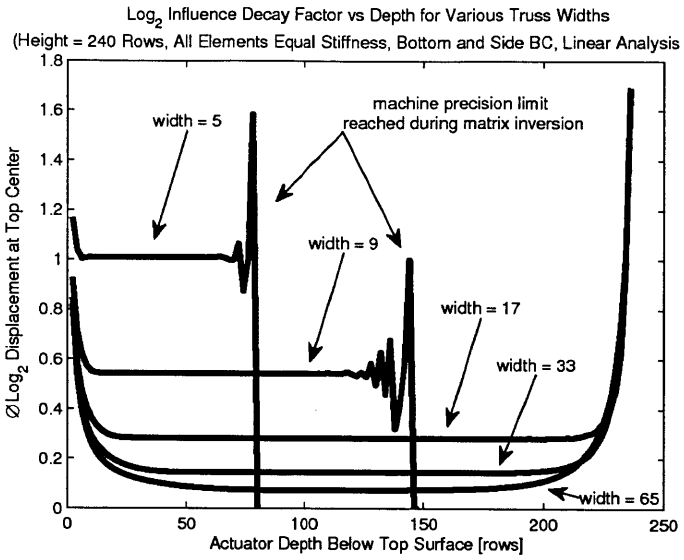

Figure 4-12: Sensitivity of Decay Rate on Truss Width with Side Boundary Condition

top surface. At the narrow extreme, the approximation of leaf springs and stacked springs used to derive the approximate influence function is in close agreement with the actual mechanics, as demonstrated by the nearly flat decay rate. At the wider extreme, the assumption breaks down and the decay rate drops.

4.3 Discussion and a Candidate Design

The numerical experiments of the previous section showed that in the planar truss there exists a region where the influence of active truss members on the vertical displacement of the top surface decays exponentially with the depth of the actuator below the top surface. The rate of this exponential decay is slightly sensitive to the stiffness ratio between the active truss members and their passive neighbors, and is much more sensitive to the horizontal distance between the active column and a stiff

reference. These two observations suggest a candidate design for a truss structure that allows optimal independent control over many adjacent degrees of freedom on the top surface of the truss, as required for optical figure correction.

A two-dimensional version of such a design is presented in Figure 4-13. This design calls for a regular triangular truss composed of three types of members. The first, shown in narrow black lines, are passive members of some nominal linear stiffness. The second, shown in thick black lines, are also passive members, but are required to be significantly stiffer than any other members in the truss. These serve to extend a "pseudo-ground" boundary condition in the vertical dimension, to allow the design to exploit the sensitivity of influence decay rate to the width between boundary conditions. Finally, there are the active elements, shown in gray lines. The linear stiffness of these active elements serves as the vernier adjustment on the decay rate coarsely defined by the lateral spacing of the stiffening columns.

Figure 4-14 plots the decay rate of actuator influences for a truss mechanism similar to the one in 4-13. This mechanism was 64 rows high, had unit stiffness passive elements, and stiffening columns 1000 times stiffer. The centers of the stiffening columns were 17 columns apart in the horizontal direction. The result shows actuator influence decay rates for various spring rates of the central actuated elements, normalized to the stroke length. While the decay rate is no longer constant, as is predicted assuming ideal infinitely stiff boundary conditions rather than stiffening columns with large but finite spring rates, the deviation from constant decay rate is low. Additionally, sensitivity of the decay rate to the stiffness ratio between the active and passive column over the region of constant decay is non-negligible, suggesting that this design can be optimized and implemented in a practical system.

As shown in Figure 4-15, this design has the property that the deformation of the top surface in response to actuation in a given "bucket" is confined to the region

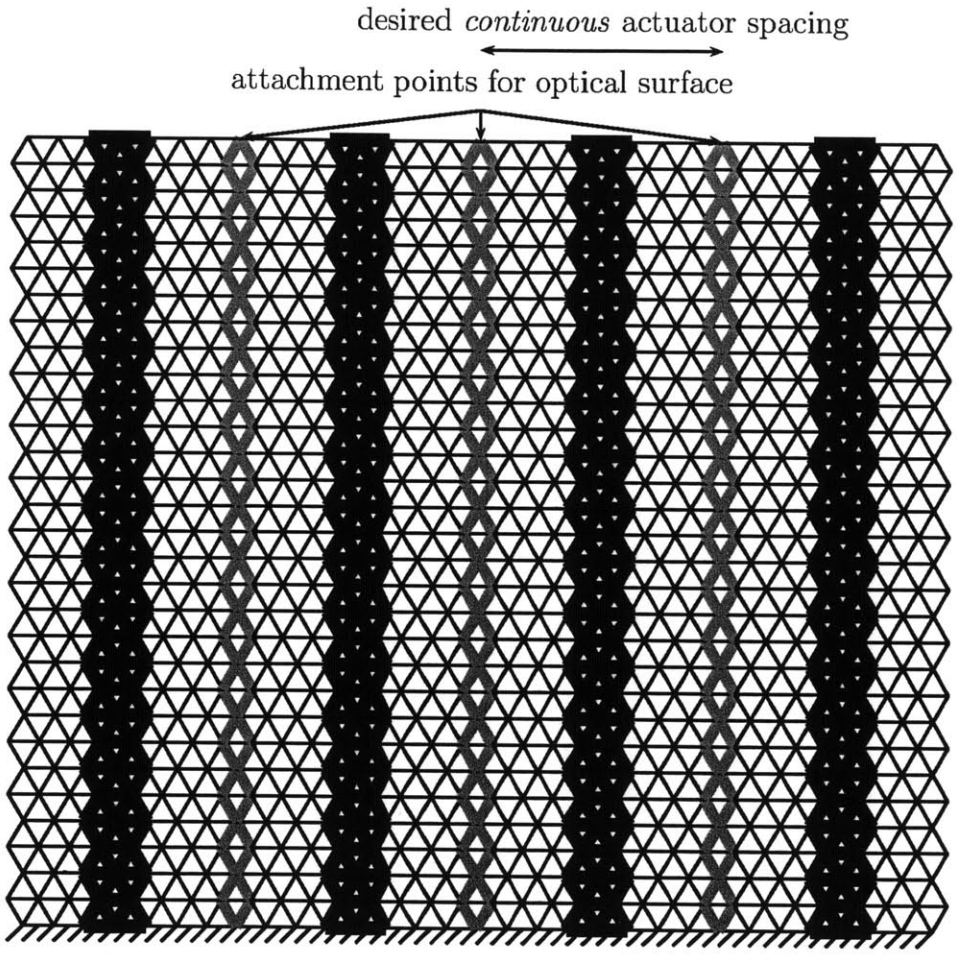

Figure 4-13: Design of Variable Stiffness Planar Truss. Bold columns represent stiffening members, gray lines are active column, think black lines are passive members.

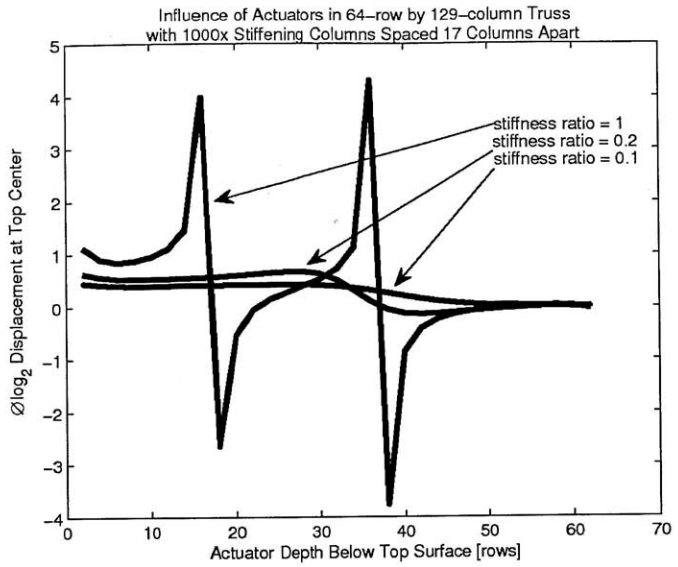

Figure 4-14: Actuator Influence Decay Rate for Truss With Stiffening Columns. Note the near-constant decay rate of ≈ 0.5 bit/row for stiffness ratios of 0.1 and 0.2.

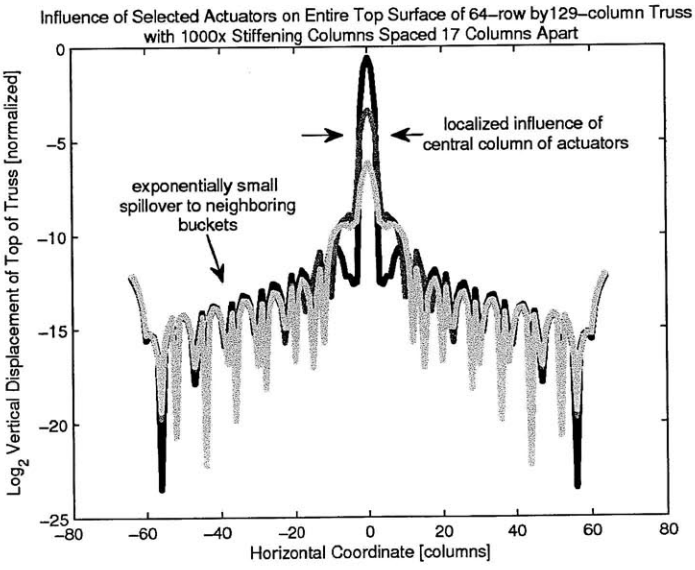

Figure 4-15: Actuator Influence on Entire Top Surface of Truss With Stiffening Columns

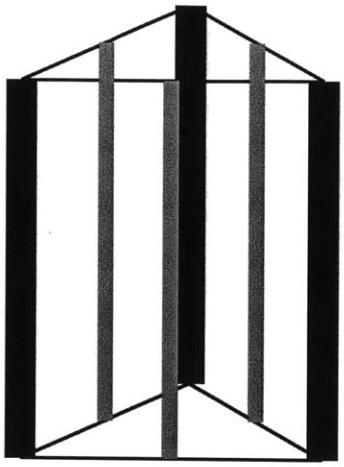

Figure 4-16: Extension of Planar Truss to Three Dimensions. The two-dimensional truss of Figure 4-13 is folded to yield a three-dimensional support for a two-dimensional optical surface.

of the surface over that bucket. This is extremely desirable, as it assures that there is little coupling between adjacent degrees of freedom.

Observe finally that this design extends trivially to three dimensions. As shown in Figure 4-16, the two-dimensional truss in Figure 4-13 can be folded around the stiffening columns and tessellated without changing the kinematics of the passive and active elements between those columns. The obvious caveat is that the stiffening columns must now be sufficiently stiff to have not only two independent degrees of freedom working against them, but six, if the triangular fold of Figure 4-16 is extended into a tight triangular packing in the horizontal plane.

Chapter 5

Conclusion

Binary mechatronics was studied in the 1990's as a design philosophy for constructing cheap, robust, robotic manipulators. Recently, proposals have been made for the application of binary mechatronics to active figure correction in large optical systems. While preliminary explorations in this direction showed promise, the kinds of methods of inverse kinematics applicable to serial robot manipulator arms do not translate well to the parallel geometries and increased actuator count in mirror support structures.

5.1 Summary of Results

The research detailed in this Thesis approaches this impasse from the vantage point of basic information theory. Knowing that practical deployed active figure correction systems in large optical telescopes correct for shape errors that require many independent degrees of freedom to parametrize, a lower bound for the information content of the figure correction system can be derived in terms of *bits*, which in

turn gives a lower bound on the minimum number of binary actuators required in an active optics system. Specifically, if, after accounting for all the natural structure in the mechanism, a corrective command *for the entire surface* needs must be parametrized by a *minimum* of N independent degrees of freedom, and each of those degrees of freedom requires a relative precision of $1/M$, the minimum number of bits required to uniquely represent any corrective action to the required precision is given by $\log_2 M^N = N \log_2 M$, corresponding to M^N discrete actuator configurations.

Knowing this lower bound on the number of required bits and corresponding number of discrete actuator configurations, the question of what the optimal distribution of those discrete configurations over the discrete workspace can be addressed. Assuming that the time-history of the required corrective action is unknown a priori, a probabilistic argument can be made that the optimal distribution of those discrete configurations is the discrete uniform distribution over the entire multi-dimensional workspace.

Knowing that the optimal distribution is uniform, and that for small inputs and to a certain tolerance, compliant binary mechatronic systems are linear in the actuator inputs, an analogy can be made between the compliant mechanism and the mathematics of independent random variables. This analogy can be used to determine the set of optimal influences of the binary actuators on the degrees of freedom of the workspace. Specifically, the optimal distribution of configurations in any degree of freedom would be achieved for a given coordinate to a relative tolerance of $1/M$ if the mechanism contains exactly $\log_2 M$ actuators with geometrically decaying influence with decay factor 2.

With this prescription in hand, mechanism compliance can be exploited to formulate designs where constant or near-constant magnitude binary actuators, corresponding to individual bits of an actuator command, have geometrically decaying

influences on the commanded measurement point. Specifically, a mathematically rigorous proof exists showing that the theoretical mechanism composed of a taught cable supported by springs has exact exponential decay of influence on the vertical displacement of a single point on the cable for constant magnitude actuators spaced at uniform intervals.

With this theoretical foundation layed, the original studies by Bilton and Lee of compliant binary-actuated truss supports for optical systems can be revisited. Confining the investigation to the linear regime, the claim is made that the statics of a large truss can be approximated roughly by the statics of the theoretical taught cable mechanism for which optimal actuator design is rigorously known to be theoretically possible. Numerical simulations confirm that actuators placed in very specific points deep in the interior of such a planar truss do indeed exhibit exponential decay of influence on the vertical displacement of the top surface, and that for suitable combinations of truss member stiffness, optimal control of multiple degrees of freedom on the top surface can be achieved with a minimal set of near constant magnitude binary displacement actuators placed at specific locations in the truss.

5.2 Future Work

This Thesis restricted its analysis to the applicability of binary mechatronics to optical systems to reject slow-moving disturbances. As such, dynamics were neglected entirely. This is may not be justified, as the design for the large truss presented in this document would most likely exhibit lightly damped ringing in response to a binary actuation in its interior.

There are several approaches to damping out vibration in trusses. The most obvious is to use stiffer or better-damped passive truss members and joints. A second

approach, studied in the early 1990's, involves placing active dampers on some truss members to slowly remove energy from vibrations in the structure [32].

Lastly, there exists a method for controlling residual vibrations in lightly-damped structures by employing a specifically designed control input time history. This control strategy is referred to in the literature as Posicast Control or Input Shaping [22]. The method was developed for suppressing residual vibration in flexible space structures. The nature of the problem this was developed to address has resulted in a sizable body of literature exploring the suppression of vibration in large flexible trusses by binary (thrust) actuation and, in particular, there exist published closed-form solutions for generating binary thrust commands of specified duration [23] that result in zero residual ringing.

At their very core, these methods are based on the idea of computing an actuator time-history where the second half of the actuation cancels the vibration induced by the first half. Given the kinds of mechanism designs dictated by the optimality criteria developed in this Thesis, a promising avenue for future research will be the application of input shaping to vibration suppression in binary mechatronic trusses.

5.3 Context

The idea of digital electronics is to trade one very precise analog component, engineered very expensively to have low noise, etc., for many components with looser tolerances. This represents two trades. One is noise immunity for rounding error. The second is increased precision for increased component count. That is, one amplifier with (say) ten transistors for one ALU with hundreds of transistors. The same trade holds in binary mechatronics. We trade one very precise (but compact) actuator for many simpler binary actuators distributed over a larger volume.

What this Thesis has brought to the discussion was the formalism to reason about these trade-offs in terms of accuracy and inverse kinematics computation time, some intuition about the kinds of mechanisms that can be constructed to exploit elastic averaging to achieve optimality in these respects, and an example of the reasoning that can be used to synthesize designs with these principles.

Bibliography

[1] P. Y. Bely, editor. *The Design and Construction of Large Optical Telescopes.* Springer, 2003.

[2] I. Bowen. Final adjustments and tests of the hale telescope. *Publications of the Astronomical Society of the Pacific*, 62(356):91–97, 1950.

[3] G. S. Chirikjian. A binary paradigm for robotic manipulators. In *Proceedings of the 1994 IEEE International Conference on Robotics and Automation*, 1994.

[4] K.-J. Cho and H. Asada. Architecture design of a multiaxis cellular actuator array using segmented binary control of shape memory alloy. *IEEE Transactions on Robotics*, 22(4):831–843, 2006.

[5] T. Cover and J. Thomas. *Elements of Information Theory.* Wiley-Interscience, 2nd ed. edition, 2006.

[6] A. Delmege and M. Tremblay. Hydraulic digital actuator. *Control Engineering*, 12:69–70, February 1965.

[7] L. M. DeVita. An mri compatible manipulator for prostate cancer detection and treatment. Master's thesis, Massachusetts Institute of Technology, 2007.

[8] L. M. DeVita, J. Plante, and S. Dubowsky. The design of high precision parallel mechanisms using binary actuation and elastic averaging: With application to mri cancer treatment. In *Proceeding of the 2007 IFToMM World Congress on Machines and Mechanisms*, 2007.

[9] D. G. Duffy. *Green's Functions with Applications.* CRC, 2001.

[10] I. Ebert-Uphoff and G. S. Chirikjian. Efficient workspace generation for binary manipulators with many actuators. *Journal of Robotic Systems*, 12(6):383–400, 1995.

[11] I. Ebert-Uphoff and G. S. Chirikjian. Inverse kinematics of discretely actuated hyper-redundant manipulators using workspace densities. In *Proceedings of the 1996 International Conference on Robotics and Automation, Minneapolis*, 1996.

[12] European Southern Observatory. Active optics, Feb. 2011. `http://www.eso.org/public/teles-instr/technology/active_optics.html`.

[13] G. Grimmet and D. Stirzaker. *Probability and Random Processes.* Oxford University Press, 3rd ed. edition, 2007.

[14] S. J. Lee. Planar feasibility study for primary mirror control of large imaging space systems using binary actuators. Master's thesis, Massachusetts Institute of Technology, 2010.

[15] S. J. Lee, A. M. Bilton, and S. Dubowsky. On the kinematics of solar mirrors using massively parallel binary actuation. In *Proceedings of the ASME 2010 International Design Engineering Technical Conferences & Computers and Information in Engineering Conference*, August 2010.

[16] D. S. Lees and G. S. Chirikjian. Inverse kinematics of binary manipulators with applications to service robotics. In *IEEE/RSJ International Conference on Intelligent Robots and Systems 95*, 1995.

[17] D. S. Lees and G. S. Chirikjian. A combinatorial approach to trajectory planning for binary manipulators. In *Proceedings of the 1996 International Conference on Robotics and Automation, Minneapolis*, 1996.

[18] Y. A. Melnikov. *Influence Functions and Matrices.* Marcel Dekker, Inc, 1999.

[19] MIT Lincoln Laboratory. *Annual Report.* 2010.

[20] E. Pearson and L. Stepp. Response of large optical mirrors to thermal distributions. *Proceedings of the SPIE*, 748, 1987.

[21] J. Plante and S. Dubowsky. The calibration of a parallel manipulator with binary actuation. In *11th Conference on Advances in Robot Kinematics (ARK)*, 2008.

[22] W. Singhose and W. Seering. *Command Generation for Dynamic Systems.* Lulu.com, 2010.

[23] W. Singhose, T. Singh, and W. Seering. On-off control with specified fuel usage. *Journal of Dynamic Systems, Measurement, and Control*, 121, June 1999.

[24] A. Slocum. *Precision Machine Design.* Society of Manufacturing Engineers, 1992.

[25] J.-J. E. Slotine and W. Li. *Applied Nonlinear Control.* Prentice-Hall, 1991.

[26] G. Strang. *Computational Science and Engineering.* Wellesley Cambridge Press, 2007.

[27] V. A. Sujan, M. D. Lichter, and S. Dubowsky. Lightweight hyper-redundant binary elements for planetary exploration robots. In *2001 IEEE/ASME International Conference on Advanced Intelligent Mechatronics*, 2001.

[28] R. Teoste, J. Daley, R. N. Capes, J. J. Alves, and M. D. Zimmerman. Measurements of tilt anisoplanatism at the firepond facility. Technical Report 815, MIT Lincoln Laboratory, 1988.

[29] S. Timoshenko and S. Woinowsky-Krieger. *Theory of Plates and Shells.* McGraw-Hill, 1959.

[30] R. K. Tyson, editor. *Adaptive Optics Engineering Handbook.* Marcel Dekker, Inc, 2000.

[31] W. M. Keck Observatory. The mirror, Feb. 2011. `http://keckobservatory.org/about/mirror/`.

[32] M. Webster, J. Fanson, B. Lurie, and J. O'Brien. Design and implementation of active members for precision space structures. In *AIAA Aerospace Design Conference*, 1992.